Neutral Pion Production in pp Collisions at $\sqrt{s} = 2.76$ TeV at the LHC with the ALICE Detector using the Electromagnetic Calorimeter

Master Thesis in Physics

Haitao Zhang
Institutt for Fysikk og Teknologi
Universitetet i Bergen

2015

under the supervision of

Prof. Dr. Dieter Röhrich

Prof. Dr. Daicui Zhou

(Central China Normal Univerity, Wuhan)

Abstract

In this thesis the measurement of the neutral pion yield and its differential invariant cross section in pp collisions at $\sqrt{s} = 2.76$ TeV is presented.

The $\pi^0 s$ are measured in the two photon decay channel and photons are reconstructed via the energy deposit in the EMCal . To obtain the π^0 yield, the strategy is to extract the signal from the invariant mass distribution of photon pairs by subtracting the combinatorial background, which is calculated mainly via the mixed events technique. The measurement of π^0 spectrum reaches to 10 GeV, being limited by the statistic and energy deposit overlap in the EMCal. Finally, the measurement is compared to the spectra measured via the Photon Spectrometer (PHOS) and that from the Photon Conversion Method (PCM) [1]. All three independent measurements agree within $\pm 10\%$, which is fully constistent with their individual sytematic and statiscal errors, and can thus be combined. The combined π^0 spectrum agrees with the NLO perturbative QCD prediction by M. Strattmann [2] and the charged pion measurement [3] at the same center-of-mass energy reasonably well.

Contents

CHAPTER 1

Physics Motivation

The measurements of neutral meson spectra in pp collisions at LHC energies present important data for perturbative QCD calculations,such as gluon fragmentation function,and provide reference to study scaling properties of hadron prodution at LHC energies,such as the nuclear modification factor at similar energies.
It is assumed that Fragmentation functions are independent of the collision system, however it needs different experiment to support. The fragmentation functions are dertemined from e^+e^- collisions at low energies which may not apply at LHC collision energies. In addition, the gluon fragmentation functions are not well constrained in electron-positron collisions,and the neutral pion is produced dominatly by gluon fragmentation. The ALICE experiment has good particle identification capabilities and it gives opportunity to test this assumption. The prodution of Neutral pions can provide avery good cross check since they can be measured over a very large momentum range.

1.1 Standard model (SM)

The Standard Model includes: Strong interaction, Weak interaction and electromagnetic interactions, while gravity is not described in the Standard Model (SM)). It contains 3 generations of quarks and leptons. As shown in the Figure 1.1. From left

to right: *Fermions*, the first generation of quarks and lepton constitute the everyday matter; The following 2 generations contain particles for exotic matters. Then the force carriers (*Bosons*): gluon of strong interaction, photon of electromagnetism, intermediate vector bosons for weak interaction. The anti-matter of fermions are not shown here, which will double the spices for these quarks and leptons (e.g. anti-u quark, $\bar{u}$ or anti-electron, positron: $\bar{e}$). They have the same properties as their anti-particles except the opposite electricity charge from each other. The anti-matter for the gauge bosons are in the same figs (E.g. the anti-photon/gluon is remain photon, anti-W^+ is W^-). The quarks (gluon) take part in strong interaction has an external freedom called "color". Quark has 3 kind of color: red(r), blue(b), green(g); while the gluon has 8 independent combine state of these r,g,b (known as "color octet"). The recent discovered "higgs", it gives mass to some of these particle introduced above (According to the gauge theory, these elementary particle should be massless). So if we count in details, the total number of particles can be considered as 61 (= 36 + 12 + 8 + 1 + 3), 36 quarks (6 flavors × 3 colors × 2 (anti-matter)), 12 lepton (6 flavors × 2 (anti-matter)), 8 gluons, photon, 3 vector bosons for weak interaction).

Three typical interactions in Standard Model are shown in Figure 1.2. The figure from left to right shows the different mediated particles in the corresponding interactions, there are respectively strong interaction by gluon, weak interaction by W^- and electromagnetic interaction by photon.

1.2 Quantum Chromodynamics

Quantum Chromodynamics (QCD) is a theory to describe the strong interaction between particle with color charge (r,g,b), like quarks and gluons. As we know, in the Quantum Electrodynamics (QED) theory, photon is to describes the electromagnetic force and as the quantum of the electromagnetic field. The role of gluon in QCD is analogous to that of the photon in QED. But the difference is the gluon itself has color charge, while photon has no (electric) charge. So it can interact with itself.
The Lagrangian of QCD is written as [4]:

$$\mathcal{L} = \sum_q \overline{\psi}_{q,a}(i\gamma^\mu \partial_\mu \delta_{ab} - g_s \gamma^\mu t^C_{ab} \mathcal{A}^C_\mu - m_a \delta_{ab})\psi_{q,b} - \frac{1}{4} F^A_{\mu\nu} F^{A,\mu\nu}. \tag{1.1}$$

where γ^μ is the Dirac γ-matrix which expresses the vector nature of the strong interaction where μ is a Lorentz vector index. $\psi_{q,a}$ are quark-field spinors to special

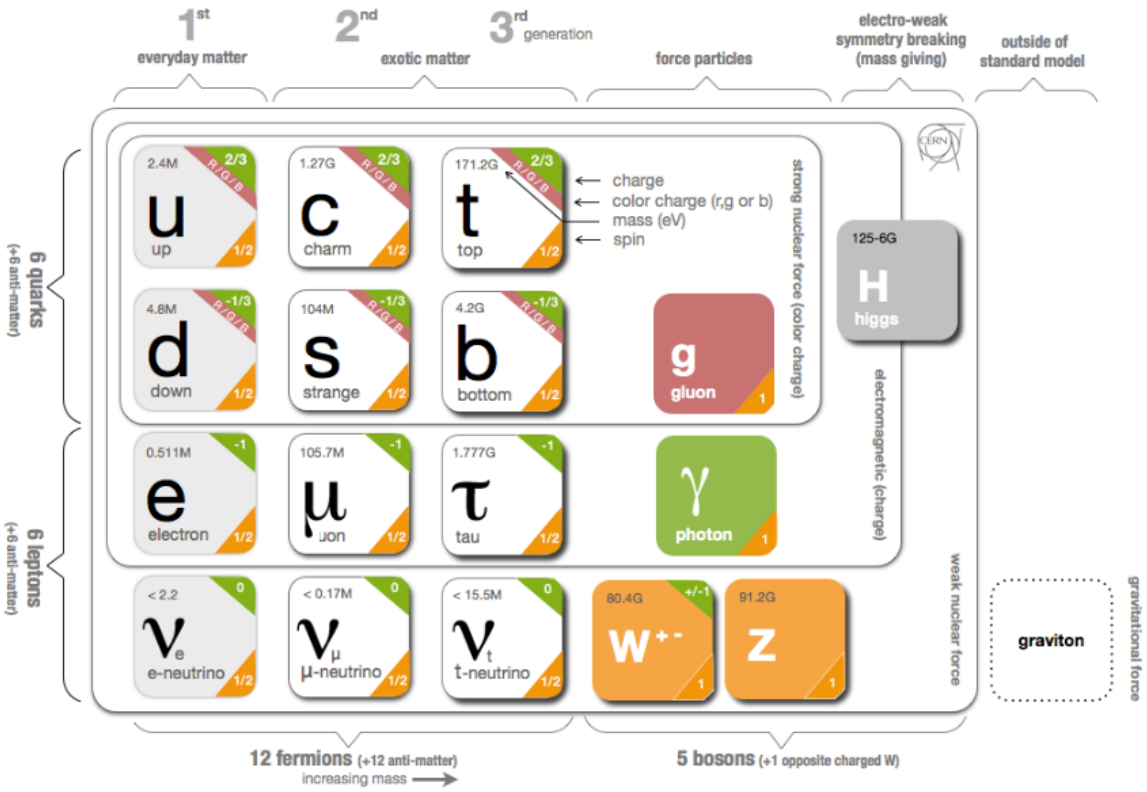

Figure 1.1: **Standard Model**: particles in Standard Model and the external graviton

flavor quark q, its mass m_q is induced by the standard Higgs mechanism. The color-index, a, runs from $a = 1$ to $N_c = 3$ since the quark is in one of the three colors. The $\mathcal{A}_\mu^C$ correspond to the gluon fields with color-index C runs from $C = 1$ to $N_c^2 - 1 = 8$ since the "color octet" of gluons in color. The t_{ab}^C are the generators of the SU(3) group with eight 3×3 matrices, written as [5]:

$$\lambda^1 = \begin{pmatrix} 0 & 1 & 0 \\ 1 & 0 & 0 \\ 0 & 0 & 0 \end{pmatrix}, \lambda^2 = \begin{pmatrix} 0 & -i & 0 \\ i & 0 & 0 \\ 0 & 0 & 0 \end{pmatrix}, \lambda^3 = \begin{pmatrix} 1 & 0 & 0 \\ 0 & -1 & 0 \\ 0 & 0 & 0 \end{pmatrix}, \lambda^4 = \begin{pmatrix} 0 & 0 & 1 \\ 0 & 0 & 0 \\ 1 & 0 & 0 \end{pmatrix}$$

$$\lambda^5 = \begin{pmatrix} 0 & 0 & -i \\ 0 & 0 & 0 \\ i & 0 & 0 \end{pmatrix}, \lambda^6 = \begin{pmatrix} 0 & 0 & 0 \\ 0 & 0 & 1 \\ 0 & 1 & 0 \end{pmatrix}, \lambda^7 = \begin{pmatrix} 0 & 0 & 0 \\ 0 & 0 & -i \\ 0 & i & 0 \end{pmatrix}, \lambda^8 = \begin{pmatrix} \frac{1}{\sqrt{3}} & 0 & 1 \\ 0 & \frac{1}{\sqrt{3}} & 0 \\ 1 & 0 & \frac{-2}{\sqrt{3}} \end{pmatrix} \tag{1.2}$$

The field tensor $F_{\mu\nu}^A$ is expressed as:

$$F_{\mu\nu}^A = \partial_\mu \mathcal{A}_\nu^A - \partial_\nu \mathcal{A}_\mu^A - g_s f_{ABC} \mathcal{A}_\mu^B \mathcal{A}_\nu^C, \tag{1.3}$$

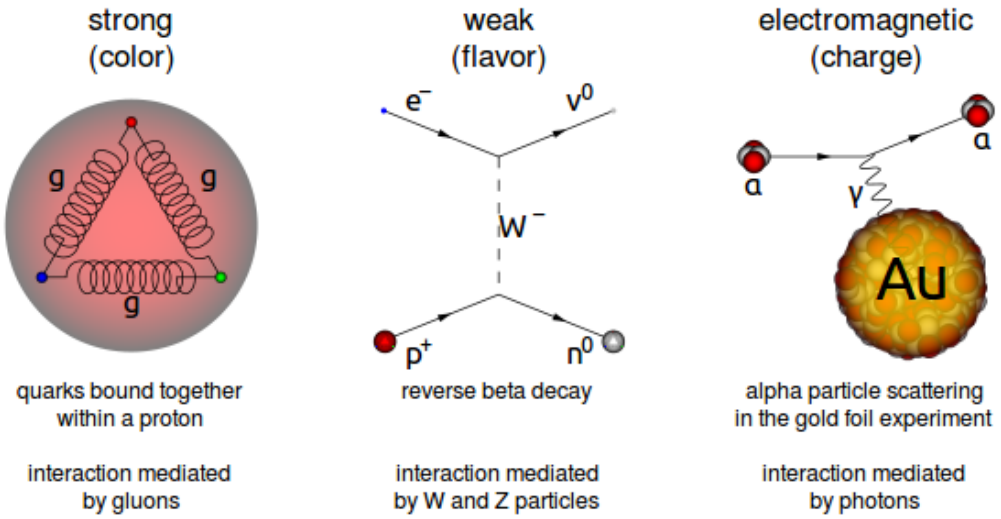

Figure 1.2: Interaction of particles in SM. The left one is the quarks bounded by gluons in a proton; The center one is so-called "reverse beta decay", electron interact with proton to create a neutron and the "missing" neutrino; The right one is the Compton scattering, α particle hit the gold.

where the definition of the SU(3) structure constant, f_{ABC}, is given by

$$[t^A, t^B] = i f_{ABC} t^C. \tag{1.4}$$

The useful color-algebra relations:

$$\begin{aligned} t^A_{ab} t^A_{bc} &= \delta_{ac} C_{\rm F} \qquad (C_{\rm F} \equiv \frac{N_{\rm c}^2 - 1}{2N_{\rm c}} = \frac{4}{3}), \\ f_{ACD} f_{BCD} &= \delta_{AB} C_{\rm A} \qquad (C_{\rm A} \equiv N_{\rm c} = 3), \\ t^A_{ab} t^B_{ab} &= T_R \delta_{AB} \qquad\qquad T_R = 1/2. \end{aligned} \tag{1.5}$$

where $C_{\rm F}$, $C_{\rm A}$ and T_R are the color-factor (known as "Casimir") associated respectively to the 3 cases as: a quark emission a gluon, a gluon emission a gluon and a gluon split to a $q\bar{q}$ pair.

The QCD coupling constant, $\alpha_s = \frac{g_s^2}{4\pi}$, which is analogous to $\alpha = 1/137$ in QED, describes the strong interaction strength. It is depending on the momentum transfer Q, the typical values as $\alpha_s \sim 0.1$ for 100 GeV-TeV range. In perturbative QCD (pQCD), α_s can be expressed as a function of an renormalization scale μ_R with [6]:

$$\mu_R^2 \frac{d\alpha_s}{d\mu_R^2} = \beta(\alpha_s) \quad = \quad -b_0 \alpha_s^2 - b_1 \alpha_s^3 - b_2 \alpha_s^4 - \ldots \tag{1.6}$$

where $b_0 = (11C_A - 4n_f T_R)/(12\pi) = (33 - 2n_f)/(12\pi)$ is referred to as the 1-loop beta function coefficient, the b_i can be calculated as the $i+1$-loop coefficient and its affect

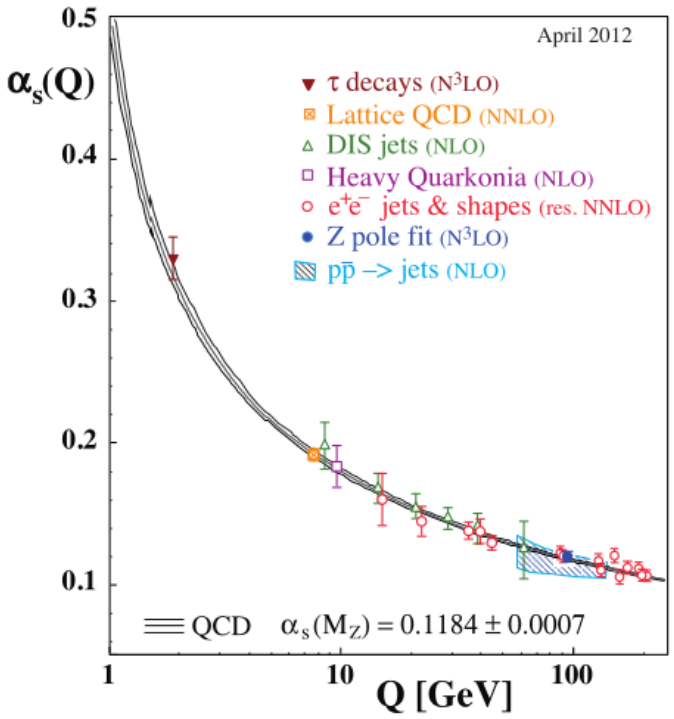

Figure 1.3: Summary of measurements of α_s as a function of the energy scale Q. The curves show the predictions from QCD at the average value of α_s between 4-loop approximation and 3-loop threshold matching heavy quark masses $M_c = 1.5$ GeV and $M_b = 4.7$ GeV. The α_s extracted from QCD perturbation are shown at next-to-leading order (NLO) (green triangles, purple squares and blue squares), NNLO (red open circles), next-to-NNLO (N^3LO) (brown solid triangle). The cross filled square in orange is based on lattice QCD. The plot is taken from [4].

decrease as the order. The fist order of in Equation 1.6 that $-b_0 < 0$ (for the number of quarks $n_f \leq 6$), shows the fact that the QCD coupling effectively *decreases* with energy, called *asymptotic freedom*. One can consider only the b_0 term at an energy range where the number of flavors is constant, under the assumption $\mu_R^2 \simeq Q^2$, written as[7, 8]:

$$\alpha_s(Q^2) = \frac{1}{b_0 \ln(Q^2/\Lambda_{QCD}^2)} \tag{1.7}$$

where Λ_{QCD} is a constant of integration, corresponding to the non-perturbative scale of QCD ($\Lambda_{QCD} \sim 1 GeV/c$). The measurements of the QCD coupling presented as a function of the energy scale Q is showed in Figure 1.3.

Figure 1.3 shows that the coupling constant α_s decrease with the momentum transfer increasing (equivalently at short distances), which is a main characteristic feature of QCD. At low momentum transfers, the coupling constant α_s is large and the perturbative approach is not valid, like what we see in the normal world, the quarks and gluons are confined in the hadrons, known as *confinement*. On the con-

trary, when α_s approaching zero, the quarks interact very weakly and can behave as if they are free. This feature of the state is of $deconfinement$, or the so-called $asymptotic\ freedom$ as we have discussed. The third characteristic associated with QCD is *chiral symmetry restoration*. The chiral symmetry exists as an exact symmetry only when the mass parameter of a quark is strictly zero. At high momentum transfers range, mass of quarks can be considered as zero, so the chiral symmetry is said to be approximately restored. However, in normal world. the quarks inside hadrons are confined and have large dynamical masses. In this case, the chiral symmetry is considered to be broken (or hidden).

1.2.1 Quark-Gluon Plasma (QGP)

In the ordinary matter, quarks and gluons exist in bounded state as "partons" in hadrons (baryons and mesons). They are confined by the strong interactions inside. As discussed in Section 1.2, the quarks and gluons could be expected to be in a deconfined state based on the asymptotic property of QCD at extremely high temperatures (high density of energy) and/or short distances (high density of mass). This deconfined state of the quarks and gluons is called Quark-Gluon Plasma (QGP), by analogy with classical plasma [9]. After the discovery of this state, one open question is about the properties of this state itself and the transition between the hadron phase to the QGP phase.

1.2.1.1 Latice QCD (LQCD)

Unlike the bounded partons in hadrons, the deconfined quarks and gluons exist at a typical energy density in QGP are considered as "free". As the increasing coupling constant requires the usage of non-perturbative methods to study the properties. A new lattice gauge theory, was proposed by K. Wilson in 1974 [10], Lattice QCD (LQCD), to solve the problem. It use a non-perturbative approach to deal with the interactions of quarks and gluons in QCD theory. In this LQCD, the QCD Lagrangian is described in Euclidean space-time lattice, where quark fields are located on the lattice points and gauge fields are defined as the links between points. The LQCD calculation provides quantitative information on the QCD phase transition between the hadron phase and the QGP phase. From the calculation, we obtain a transition at baryonic potential $\mu_B = 0$ for massless quarks, which agrees with the spontaneous breaking of the chiral symmetry in QCD. The estimated phase transition temperature (or called the critical temperature, T_c) is at $T_c \sim 170$ MeV,

and the corresponding density of energy is at $\varepsilon = 0.7$ GeV/fm^3 [11]. We can see the left panel of Figure 1.4.

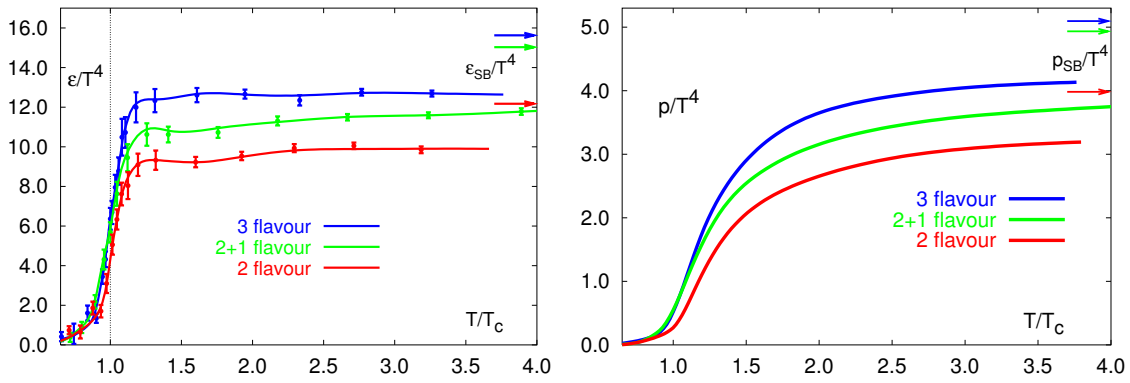

Figure 1.4: **Left:** Scaled energy density ε/T^4 as function of temperature T from lattice calculations. **Right:** Scaled pressure p/T^4 in QCD with different number of degrees of freedom as a function of temperature T. Both calculations are carried out with 2 or 3 light flavors or 2 light and 1 heavy flavor (s-quark). The arrows are the predictions with Stefan-Boltzmann limit corresponding to different number of flavors.

The QCD pressure can approach to the ideal QGP phase value at infinite temperature due to the asymptotic freedom of QCD. As shown in the right panel of Figure 1.4, the pressure strongly depends on the number of degrees of freedom [12]. Both of these calculations are based on $16^3 \times 4$ lattice and used the p4-improved staggered quark action with the Symanzik improved gauge [12]. A clear number of flavors dependence is observed for energy density and pressure, which becomes larger when going to larger number of degrees of freedom.

1.2.1.2 QCD Phase diagram

The QCD phase diagram is shown in Figure 1.5. The various phases including vacuum, hadron gas, nuclear matter, color superconductor and Quark-gluon plasma are in white. The critical point and crossover are presented by a smeared point and dash lines, respectively. Some experiment regions also are shown in the phase diagram with yellow marks.

Normal nuclear matter, such as Pb (82 protons and 126 neutrons) or Au (79 protons and 197 neutrons), have a low T and $\mu_B \sim 900$ MeV. There, the quarks and gluons are confined in neutrons and protons. These hadron (proton/neutron are baryon, one specie of hadron) can be thought as a bag packed partons together inside. But when

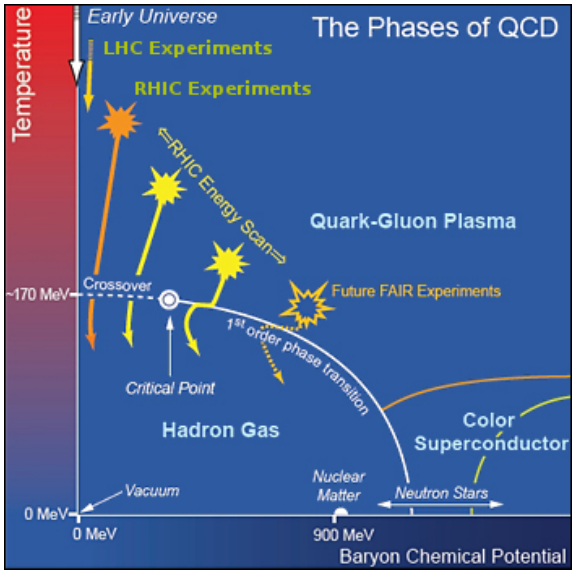

Figure 1.5: Schematic of the QCD phase diagram of nuclear matter in terms of the temperature (T) versus baryon chemical potential (μ_B). The solid curve in white shows the phase boundaries for the indicated phases. The big solid circle depicts the critical point where the sharp distinction between the hadronic gas and QGP phases blurs (extend from/to crossover). Possible trajectories for systems created in the QGP phase at different accelerator facilities are also presented (RHIC, LHC, FAIR...).

under extreme conditions, like high temperature or high baryon chemical potential (or both), quarks and gluons become free. This is the well known deconfinement partons, which cause the phase transition from hadrons gas to the quark-gluon plasma. The deconfinement at large baryon chemical potential is considered to exist in the interior of neutron stars [13] and color superconductor [14], where the density of the nuclear matter is compressed more than 10 times as the normal nuclear density. And the deconfinement of nuclear matter can be achieved by colliding heavy nuclei at enormous energies, *i.e.* SPS, RHIC and LHC. The first few moments in the small region of the collision, the temperature can achieve to lager than a critical temperature of $T_c \approx 170$ MeV, thus the QGP would be created.

From the phase diagram, we can see that on the both sides of first order phase transition line (where deconfinement occurs), the phases of the matter are shown as hadron gas (lower T) and quark-gluon plasma (higher T). The transition line starts at a point known as the QCD critical point [15]. From the point, both phases are distinct and the transition from one phase to the other is sharp. Otherwise, both of them can co-exist and the transit from one to the other in a smooth crossover [16]. There is now considerable evidence that the universe began as a fireball, called the

"Big-Bang". It is believed that after the electro-weak transition ($t \sim 10^{-11}$ s and $E \sim 1$ TeV), the QCD phase transition happened at $t \sim 10^{-6}$ s. Therefore, studying the phase transitions of quark-gluon plasma also helps to understand the behaviour of matter in the very early universe.

CHAPTER 2

Experimental setup

In this chapter, an overview of the experimental setup used for this analysis work will be presented. The first section is dedicated to the accelerator system. In the latter section, the ALICE (A Large Ion Collider Experiment) detector system and its sub-detectors which are involved in this analysis work, are introduced in detail.

2.1 Large Hadron Collider (LHC)

The Large Hadron Collider (LHC) at CERN (European Organization for Nuclear Reasearch) is located on the border between Geneva, Switzerland and France.So far,it is the largest and man-made highest-energy particle accelerator with a circumference of 27 km, at a depth ranging from 50 to 175 m beneath the earth's surface.

There are two adjacent parallel beamlines (beam pipes) which are kept at ultra-high vacuum in the accelerator. Inside the beamlines, two particle beams travel in opposite directions at the speed very close to speed of light till they are made to collide at four main points (P1, P2, P5 and P8) in the LHC, see Figure 2.1.

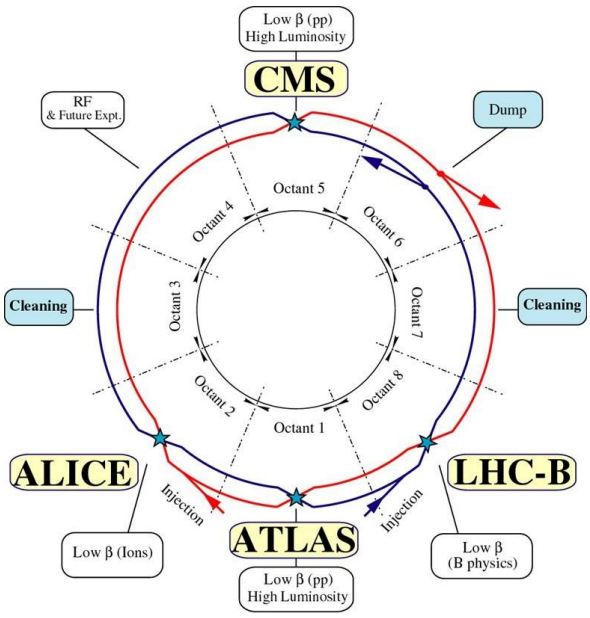

Figure 2.1: Layout of the LHC sectors and the interaction points . The two hadron beams, going in clockwise (Beam 1) and anticlockwise (Beam 2) directions, are shown in red and blue [17].

2.2 ALICE detector overview

A Large Ion Collider Experiment (ALICE) is one of four large detector systems at the CERN LHC. The detector was built by international collaboration which over one thousand physicists and engineers coming 138 institutes in 36 countries contributed in.

It has been designed to investigate the strongly interacting matter and the quark-gluon plasma created at extremely high energy densities and temperatures in nucleus-nucleus collisions, so that parton kinematics and energy in the plasma phase and jet suppression can be studied. The temperature of the quark-gluon plasma can be derived by measuring the prompt photons. However, not only the nucleus-nucleus collisions are investigated,but also the proton-proton and proton-nucleus collisions are investigated since they will be used as the reference data for heavy ion collisions. Figure 2.2 shows the schematic layout of ALICE detector.

The detector setup consists of three parts including a central barrel detector system, several forward detectors and a muon spectrometer [18, 19]. An overview of the pseudo-rapidity η coverage of the ALICE system is shown in Figure 2.3.

In the following sections, the detectors which have been used in the presented data analysis, ITS, TPC, VZERO and EMCal, are described in details. A little description is also given briefly to the other detectors.

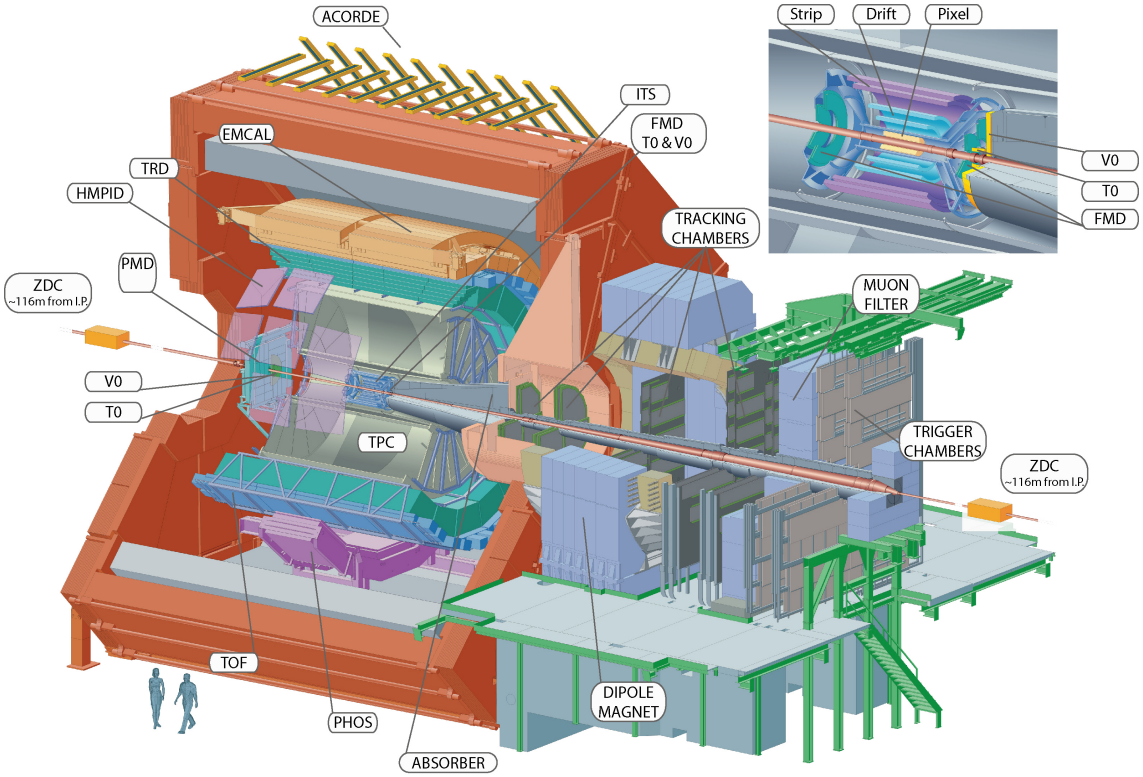

Figure 2.2: ALICE schematic layout.

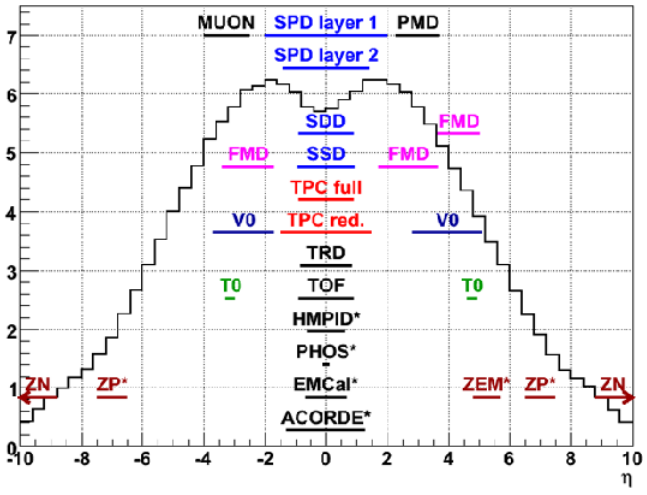

Figure 2.3: Overview of the pseudo-rapidity acceptance of ALICE sub-detectors [20].

2.2.1 Inner Tracking System (ITS)

The Inner Tracking System (ITS) [21], which is placed close to the interaction region, is composed of three different silicon detectors (SPD, SDD, SSD) with two layers (each silicon has two layers) around the beam pipe at distances between 4 cm and 44 cm. It roughly covers the pseudo-rapidity range of $|\eta| < 0.9$ and has full azimuthal coverage for all collision vertices located within $\pm 1\sigma_z$ length of the beam-beam interaction region (± 5.3 cm along the beam direction) (see Figure 2.1).

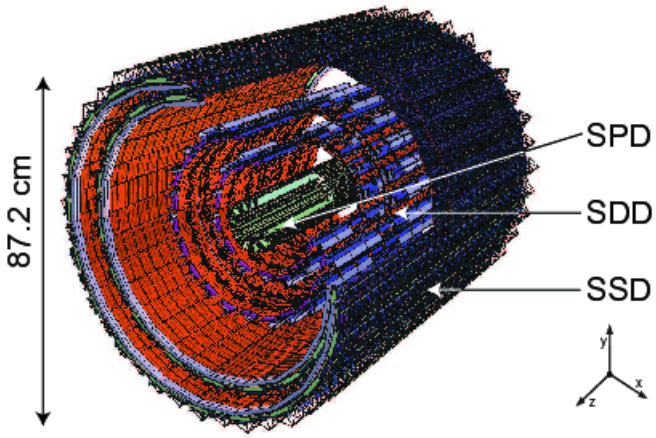

Figure 2.4: Schematic view of the ITS. It consists of three silicon detectors, SPD, SDD and SSD, with each having two layers.

The first two layers of the ITS make up the Silicon Pixel Detector (SPD). They are located at an average distance of 3.9 cm and 7.6 cm from the beam axis, respectively. The SPD is crucial for determination of the position of the primary vertex, as well as the measurement of the impact parameter of secondary tracks from the weak decays of strange, charm and beauty particles. The two intermediate layers of ITS, Silicon Drift Detector (SDD), are at the average radius of 14.9 cm and 23.8 cm, where the charged particle density is already smaller, expected to be about 7 cm^{-2}. The outer two layers, constructed from double-sided silicon micro-strips, are positioned at 38 and 43 cm, called Silicon Strip Detector (SSD). A summary on the six silicon detector layers of the ITS can be found in Table 2.1 [21]
The measured impact parameter resolution of the ITS is presented in Figure 2.5.

2.2.2 Time Projection Chamber (TPC)

The Time Projection Chamber (TPC) [24] is the main tracking detector which is a cylinder shaped chamber surrounding the ITS. The inner radius of it is 84.8 cm and

Layer	Radius (cm)	$\pm z$ (cm)	$\lvert\eta\rvert$	$\sigma_{r\varphi}$ (μm)	σ_z (μm)
1 (SPD 1)	3.9	14.1	1.98	0.266	100
2 (SPD 2)	7.6	14.1	0.9		
3 (SDD 1)	14.9	22.1	0.9	35	25
4 (SDD 2)	23.8	29.7	0.9		
5 (SSD 1)	38.0	443.1	0.9	20	830
6 (SSD 2)	43.0	48.9	0.98		

Table 2.1: Summary on the six silicon detector layers of the ITS [18, 21].

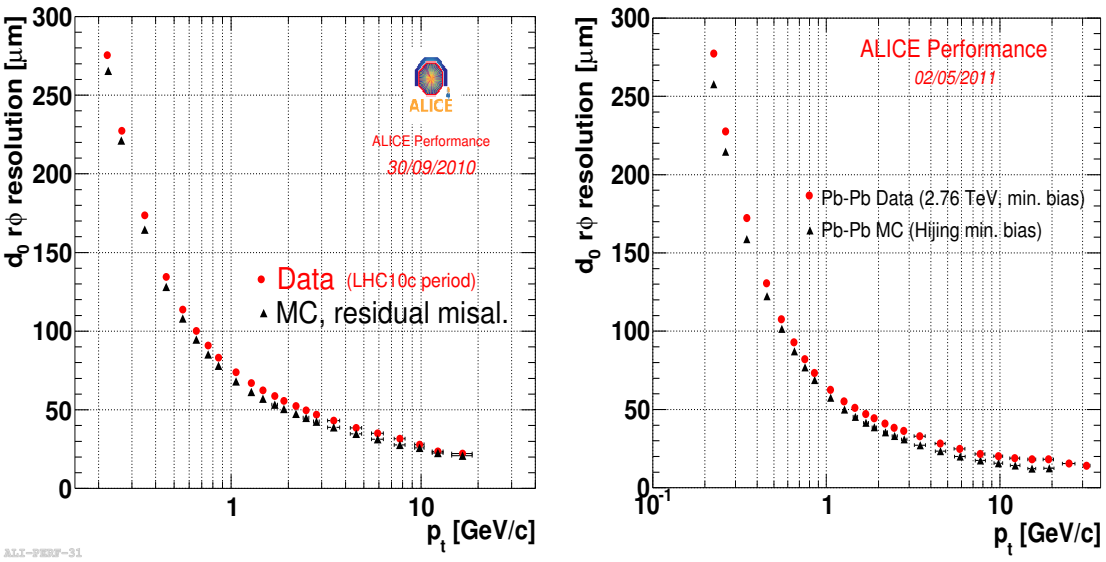

Figure 2.5: Impact parameter resolution of ITS+TPC tracks for proton-proton [22] (left) and lead-lead collisions [23](right). Data (red) has been compared with Monte-Carlo simulations (boxes) with residual misalignment has been introduced

an outer radius is 246.6 cm , the total length in the z direction is about 500 cm. Due to this design the dE/dx resolution is better than 10%. Due to is large extensions in z-direction the TPC has an acceptance in pseudo-rapidity of $-0.9 < \eta < 0.9$. The detector shape is shown in Figure 2.6. The detector is made of two main components: the cylindrical field cage which provides a uniform electrostatic field is filled with 90 m^3 gas mixture of Ne/CO_2 (90%/10%). As a result, the field cage can be used at very high-voltage gradients, of about 400 V/cm, with a high voltage of 100 kV at the central electrode with which a maximum drift time of about 90 μs can be achieved.

The readout chambers are installed at the two end-caps of the TPC cylinder with an overall active area of 32.5 m^2. They are multi-wire proportional chambers with cathode pad readout. Since the TPC is the main tracking detector of the ALICE

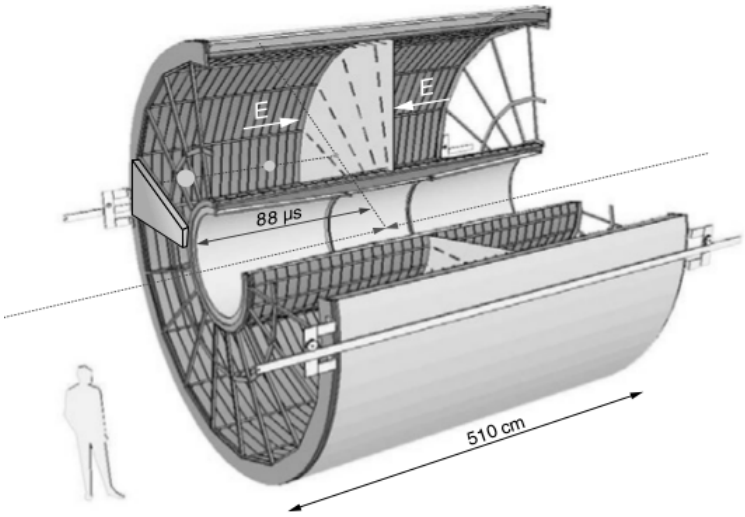

Figure 2.6: Schematic view of the TPC. TPC detecter with the inner radius of 84.8 cm and the outer radius of 246.6 cm in in the pseudo-rapidity $-0.9 < \eta < 0.9$.

central barrel together with the other central barrel detectors, ITS, TRD, and TOF, it can be used for charged-particle momentum measurements, particle identification through dE/dx measurement, studies of hadronic and leptonic signals, as well as vertex determination. On one hand ,the TPC can measure tracks of charged particles with transverse momenta from 0.1 GeV/c up to 100 GeV/c. On the other hand, the TPC can identify particles by measuring the specific energy loss in the gas. It provides identification particles from the low-momentum region up to few tens of GeV/c, in combination with ITS, TRD and TOF. The dE/dx measurement in the TPC with global tracks in pp collisions and Pb–Pb collisions are shown in Figure 2.7.

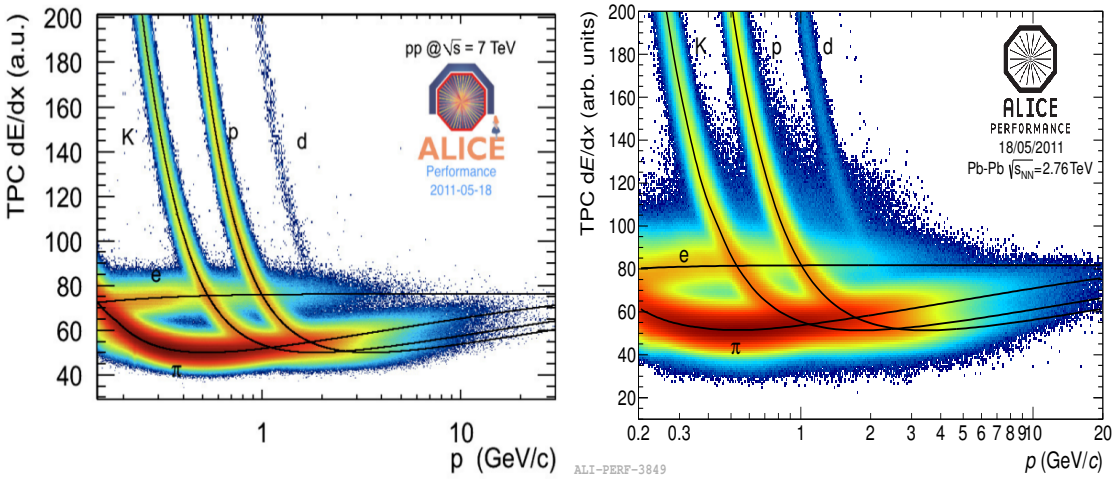

Figure 2.7: The dE/dx measured in the TPC in pp collisions (left) and Pb–Pb collisions (right). The continuous black curves comes from the Bethe-Bloch parametrization represent for different particles.

2.2.3 PHOton Spectrometer (PHOS)

The PHOS [25] is a high-resolution high-granularity electromagnetic spectrometer covering a limited acceptance . It consists of a highly segmented electromagnetic calorimeter, which is placed at the bottom of the ALICE setup at a distance of 460 cm from the collision vertex and covers in pseudo-rapidity, $-0.12 < \eta < 0.12$, and $220^\circ < \phi < 320^\circ$ in azimuthal angle with five modules presently only three modules are installed covering $260^\circ < \phi < 320^\circ$. Each PHOS module is segmented into 3584 detection cells arranged in 56 rows of 64 cells. The detection cell consists of a $22 \times 22 \times 180$ mm lead-tungstate crystal, $PbWO_4$ (PWO), coupled to a 5×5 mm Avalanche Photo Diode (APD) followed by a low-noise preamplifier [26], see the left panel of Figure 2.8. The PWO crystal is designed with this geometry corresponding to $20X_0$ radiation length in the longitudinal direction, which is known as its characteristics of the fast signal and the small Moliere radius of about 2 cm. The right pannel of Figure 2.8 shows the obtained energy resolution as a function of photon energy together with previous results from the prototypes [26, 27] and a fitting result by following formula:

$$\frac{\sigma}{E\ (\mathrm{GeV})} = \sqrt{\frac{0.018}{E} \oplus \frac{0.033}{\sqrt{E}} \oplus 0.011} \tag{2.1}$$

Therefore,the PHOS detector is designed to identificate photons, electrons and

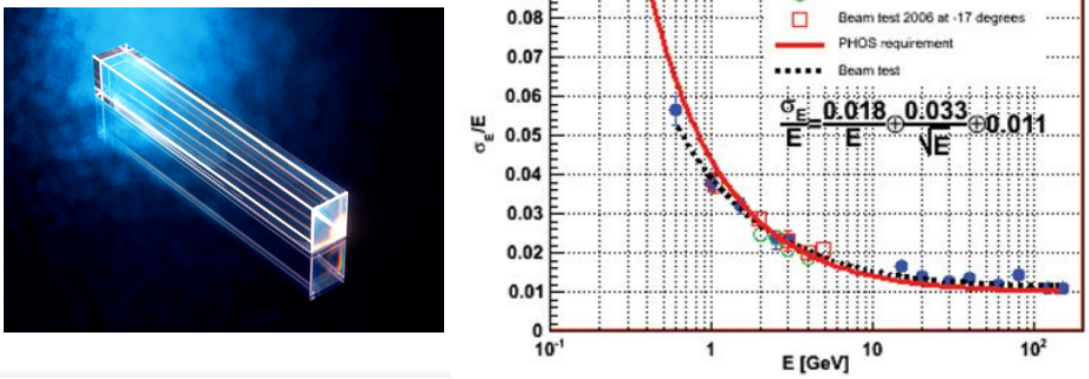

Figure 2.8: Left: $PbWO_4$ crystal in the PHOS module. Right: Energy resolution.

positrons because its fast response and very good position and energy resolution.

2.2.4 Electromagnetic Calorimeter (EMCal)

The Electromagnetic Calorimeter (EMCal) is a sampling calorimeter in ALICE. It is designed to measure the energy of a neutral particle. The calorimeter design incorporates a moderate detector average active volume density of ~ 5.68 g/cm^3 which results from a $\sim 1 : 1.22$ Pb to scintillator ratio by volume. This results in a compact detector consistent with the EMCal integration volume at the chosen detector thickness of 24.6 cm$\sim$ 20 radiation lengths.
The full acceptance of EMCal consists of a barrel section providing coverage for a 107° (80° $\sim$ 187°) arc in azimuth (in ϕ) and 1.4 units (-0.7 $\sim$ 0.7) of pseudo rapidity (η) along the beam direction. See Figure 2.9.

When a particle hits the calorimeter, it will create an electro-magnetic shower caused by its interaction with the scintillator (and the particles generated in cascade from this) while punching through. The shower contains photons, electrons and positrons. During these interactions, the emitted photon was from the decay of exited state of electron in the atom, therefore contains a certain frequencyenergy. These photons will be transport by fibers in EMCal, and be collected by the APD (Avalanche PhotoDiode) at end. By multiplying the sum the energy/number of these photons in the shower and the sampling factor (by the electronics of EMCal), we get the energy of the incoming particle. Because the tower thickness of $\sim$ 20 radiation lengths. It gives a maximum deviation from linearity (due mainly to shower

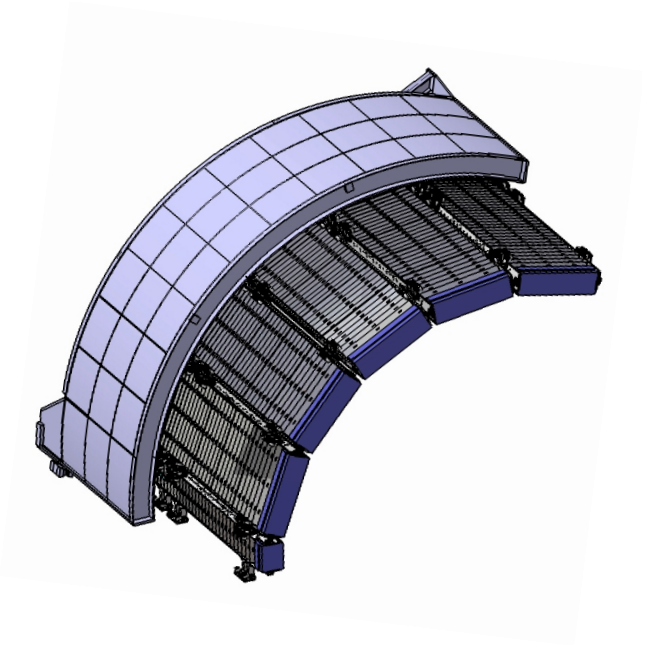

Figure 2.9: Full EMCal geometry, 10 SM and 2 "narrow" (1/3 size in ϕ of) SM in extension

leakage) of $\sim$ 2.8% for the most probable energy response in the range up to 100 GeV photons in simulations. Tower size consist 95% of effective Moliere Radius.

2.2.4.1 Structure of EMCal

EMCal is built up from 10 "Super Modules" (SM, covers 20°in *phi*, 0.7 in η each) and 2 SM in extension, which is 1/3 of the normal one in ϕ direction. Each SM consist 288 modules, 12 (in ϕ) $\times$ 24 (in η), while the SM in extension contains 4 (in ϕ) $\times$ 24 (in η), 96 in total. Each module is divided into 4 (2 $\times$ 2) "towers/cells". So there are a total of 12,288 separate towers in the full detector. Each of these towers is a basic detection sensor of the detector capable of high-resolution measurements of electromagnetic energy.
The installation of the super module is to arrange them as 24 "strip module" in η. See Figure 2.10 (left).

Each of these Strip Modules contains 12 (4 for the super modules in extension) modules parallel in ϕ. They are the same orientation in the plane constitute of y and z axis. Then install each "strip module" in super module with a typical angle which make them toward to the interaction pointin ϕ plane. See Figure Figure 2.10 (right). Every 4 towers in one module are bounded together with Aluminium plate for in-

Quantity	Value
Tower Size (at η=0)	$\sim$6.0 $\times$ $\sim$6.0 $\times$ 24.6 cm^3 (active)
Tower Size	$\Delta\phi$ x $\Delta\eta$ = 0.0143 x 0.0143
Sampling Ratio	1.44 mm Pb / 1.76 mm Scintillator
Number of Layers	77/76 layers of Scintillator/Pb
Effective Radiation Length X_o	12.3 mm
Effective Moliere Radius R_M	3.20 cm
Effective Density	5.68 g/cm3
Sampling Fraction	10.5
Number of Radiation Lengths	20.1
Number of Towers	12,288
Number of Modules	3072
Number of Super Modules	10 full size, 2 one-third size
Total Coverage	$\Delta\phi = 110^o$, -0.7 $< \eta <$ 0.7

Table 2.2: The EMCal Physical Parameters.

stallation. Each tower is made as a sandwich of 77 layers of scintillator (for creating electronic shower) and paper (serves as a diffuse reflector on the scintillator surfaces and provides friction between layers[28]) and 76 layers of lead(for absorbing the energy of incoming particles). 1.44 mm Pb and 1.76 mm scintillator. There are 6×6 = 36 fibers in each tower to collect the photons for one APD in the upper end.

2.2.4.2 EMCal Trigger

For a better selection of events we use EMCal as Trigger for its fast response. The EMCal L0/L1 trigger for photons and electrons is the same as for PHOS, as the same Front End Electronics (FEE) is used. The FEE generates fast analogy of a 2×2 tower sums which are then summed in the FPGA of the Trigger Region Unit (TRU) into 4×4 regions for high energy shower trigger decisions at L1. The output will be transmitted to the Summary Trigger Unit (STU) at a decision rate of 40 MHz.

2.2.4.3 Clusterizers

There are a variety of strategies to combine EMCal cells to form clusters. Some basic concepts, designated $v1$, $v2$, NxN, and $v1 + UF$ are outlined below:

v1 Clusterizer

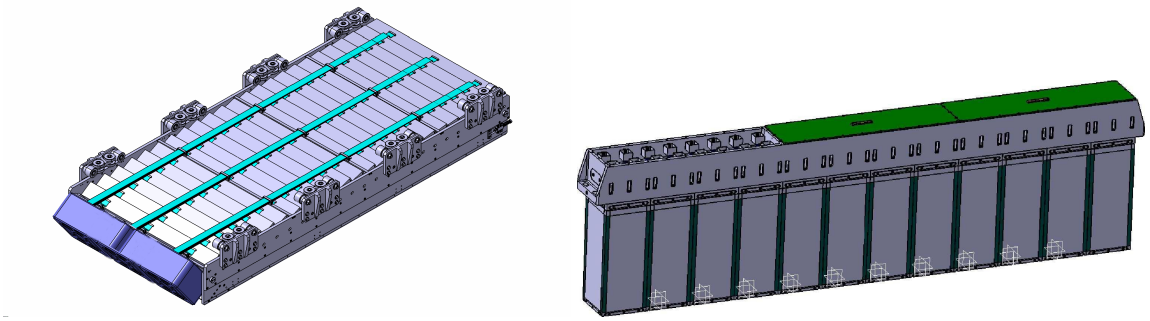

Figure 2.10: Left: One of standard Super Modules in EMCal. The upper surface (with green cables) is the one farther from the interaction point. 24 Strip Modules with a different orientation each in it, oration more 1.5°than previous one. Their lower edges are in one plane in the lower surface. Right: There are 12 (4 for ones in EMCal extension) modules in a Strip Module. This is the cross section with 2 towers in neighbourhood, as a module, is a isosceles trapezium.

The $v1$ clusterizer searches for a cell with $E_{cell} \geq clust_{threshold}$ and uses this cell as a seed for the cluster. It then adds all cells with $E_{cell} \geq cell_{threshold}$ which share a common side with the cluster. This algorithm continues until there are no remaining cells to add to the cluster. The center of gravity of the energy of the cells is calculated to determine the cluster position. The cells are then removed from any further clustering; no cell can be in two clusters! The $v1$ clusterizer is ignorant of the concept of splitting merged clusters.

NxN Clusterizer

The NxN clusterizer is a simple attempt to separate clusters which may be merged. Typically, $N = 3$ and square clusters are formed. NxN looks for the highest energy cell (with $E_{cell} \geq clust_{threshold}$) and then adds the 8 (in the case of $N = 3$) surrounding cells to it. These cells are then removed from further clusterization; a cell can only belong to 1 cluster!

v2 Clusterizer

The $v2$ clusterizer is similar to the $v1$ clusterizer but also attempts to disentangle some merged clusters. This is accomplished by looking for a change in the derivative of the deposited energy as the cluster grows. If the candidate cell has more energy than it's adjacent cluster cell then it is *not* added to the cluster and the algorithm terminates. When searching for a seed cell, the $v2$ clusterizer starts with the highest energy cell in the calorimeter. As in $v1$, clustered cells are subsequently removed from further clustering and can only

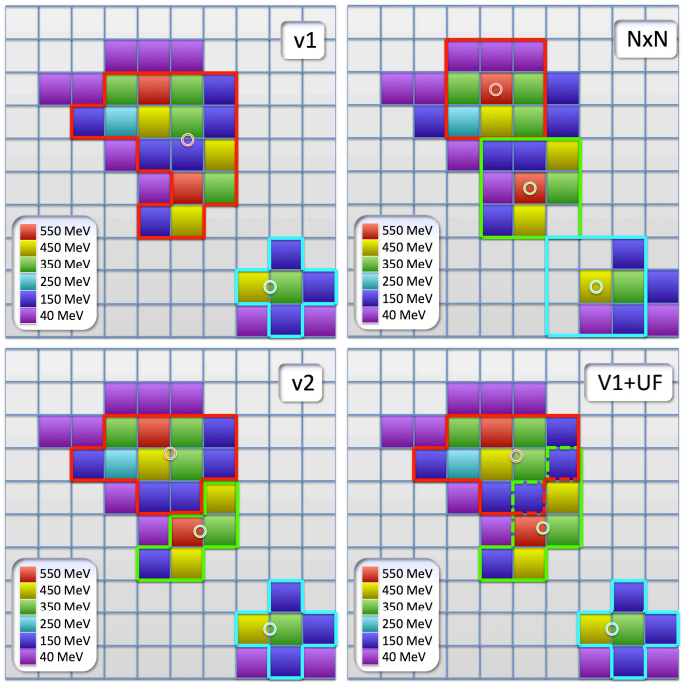

Figure 2.11: An illustrative example of how the $v1$, $v2$, NxN, and $v1 + UF$ clusterizers would group cells into clusters. The boxes show which cells belong in a given cluster and the circles approximate the assigned cluster position. This is using a clustering threshold of 300 MeV and a cell threshold of 50 MeV and $N = 3$.

be associated with one cluster.

v1 + unfolding Clusterizer

The $v1+UF$ clusterizer is similar to the $v2$ clusterizer. The primary difference is that it allows the low amplitude cells which bridge the two merged clusters to be split between the two clusters. The energy is divided based on a shower shape profile of each merged cluster.

An illustrative example of the various clusterizers is shown in Figure 2.11. This is a toy example with made up cells meant only to convey the conceptual differences between the algorithms. The clustering threshold is $clust_{threshold} = 300$ MeV and the cell threshold is $cell_{threshold} = 50$ MeV. The NxN example uses $N = 3$.
The two main clusterizer parameters that are tuned in this analysis are the clusterizer type (ie. $v1$, $v2$, etc) and the clustering threshold ($clust_{threshold}$). Within this note the clusterization schemes are referred to by $[clust_{threshold}][type]$ (ie. $100v1$ means $v1$ clusterizer with a 100 MeV clusterization threshold).

2.2.5 VZERO

The VZERO [29] is a small-angle detector consisting of two arrays of scintillator counters placed at two sides of the ALICE interaction region. One is named VZERO-A (V0-A) device which is located on the positive z-direction at a distance of about 340 cm from the interaction point while the other is named VZERO-C (V0-C) device which is placed at the negative$z$-direction along the absorber nose at 90 cm from the interaction point. The two counters have the pseudo-rapidity coverage $2.8 < \eta < 5.1$ (VZERO-A) and $-3.7 < \eta < -1.7$ (VZERO-C). Both of V0-A and V0-C are segmented in four rings. Each ring covers 0.4-0.6 unit of pseudo-rapidity. For the A-side, 32 elementary counter are distributed while for the C-side, 48 elementary counters are arranged with 8 counters on the two inner rings and 16 counters on the two outer rings.

CHAPTER 3

Neutral Pion Reconstruction

This part describes the measurement of the neutral pion invariant cross-section as a function of transverse momentum (p_{T}) in pp collisions at $\sqrt{s} = 2.76$ TeV. The general strategy is to look in the channel $\pi^0 \to \gamma\gamma$ by measuring the two decay photons in the EMCal. This branching ratio accounts for approximately $98.823 \pm 0.034\%$ of all π^0 decays. The π^0 mass is 134.977 ± 0.001 MeV/c^2 and it's lifetime (τ) is $(8.52 \pm 0.18) \times 10^{-17}$ seconds, corresponding to $c\tau = 25.5$ nm. Therefore, effectively, every π^0 decays immediately after it's created.
The mass and transverse momentum of the π^0 candidates are calculated as

$$m^2_{\pi^0} = 2p_{\gamma_1}p_{\gamma_2}(1 - \cos\theta) \tag{3.1}$$

$$p^2_{T,\pi^0} = (p_{x,\gamma_1} + p_{x,\gamma_2})^2 + (p_{y,\gamma_1} + p_{y,\gamma_2})^2 \tag{3.2}$$

where θ is the opening angle between the two photons.
Conventionally all photon candidates (so-called clusters) reconstructed in the EMCal are combined and the invariant mass is calculated, as there is no inherent way to determine whether cluster i and cluster j are from the same parent π^0 and should thus be paired together. Afterwards the combinatorial background is statistically subtracted. To estimate the relative amounts of signal and background as a function of p_{T}, Figure 3.1 plots the estimated signal divided by signal plus background. The signal estimation is described in Section 3.4 while the signal plus background is

simply the raw mass distribution. The comparison is done via the integral of each between $\pm 2\sigma$ of the fit π^0 peak. This quantity saturates at unity when there is absolutely no background.

However for this method one must be able to spatially resolve each of the individual

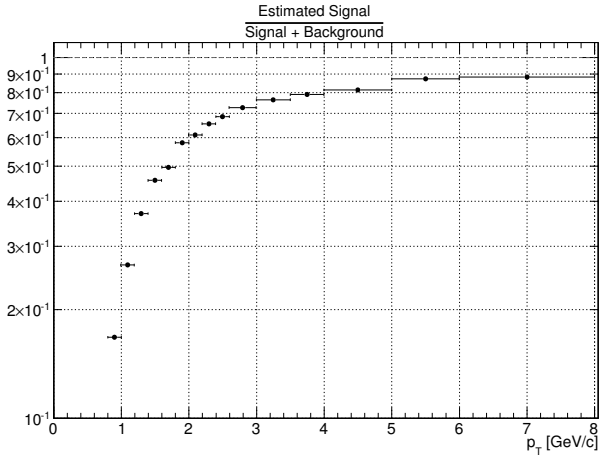

Figure 3.1: The estimated signal divided by the signal+background for π^0 as a function of transverse momentum between $\pm 2\sigma$ of the fitted π^0 peak. Estimated using data from the first data taking period for pp collisions at $\sqrt{s} = 2.76$ TeV in 2011.

photons. If θ is too small then it's possible that the energy depositions in the calorimeter will overlap causing the photons to appear "merged." In such a case, the two photons appear as a single high energy photon and the π^0 would be lost. The threshold for this merging of clusters depends highly on the algorithm to reconstruct the clusters. In the ALICE EMCal several clusterizers are used, as explained in Section 2.2.4.3. The coursest of the clusterizers (V1) starts merging photons at ~ 6 GeV and becomes fully inefficient even for asymmetric decays at ~ 15 GeV. For the V2 and the V1+unfolding clusterizers these boundaries are pushed out to ~ 12 and ~ 25 GeV respectively.

In the following sections the data set and Monte Carlo productions used in this analysis will be described first. Afterwards the signal extraction and the necessary corrections will be discussed. Finally the obtained invariant cross section will be presented and compared to theory calculations by Marco Strattmann [2] and Pythia 8 calculations.

3.1 Authors contribution

The results presented in this thesis are based on the analysis note "ALICE-ANA-2013-1024" which is a joint analysis note written by Jason Kamin and the author of the thesis. The author is involved in the neutral-meson EMCal working group since the start. The main analysis cuts applied in the analysis are based on the author's work, as well as the vertex finding efficiency results from the studies of the author. The energy non-linearity correction based on the symmetric decay method was contributed by Jason, as well as the correction for secondary pions. The presented final measurement are from the team work of the author and Jason. The systematic uncertainties are based on the author's initial studies and then further improved by Jason. The achieved analysis results have been compared to results from measurements of π^0 by ALICE PHOS and PCM group.

3.2 Data Sets and Monte Carlo Simulations

ALICE started collecting data from proton-proton (pp) collisions in November 2009. Since then pp collisions have been recorded at four different center-of-mass energies ($\sqrt{s} = 0.9$, 2.76, 7 and 8 TeV). Moreover, ALICE collected data for Pb–Pb and p–Pb collisions. In this thesis only data taken for pp collisions taken at $\sqrt{s} = 2.76$ TeV will be considered. The data taking is split into so called periods, which each corresponds to approximately a month of data taking and extends in between two technical stop, which allow repairs or adjustments to the detectors. The considered period was taken in March 2011- April 2011 and is called LHC11a, it has been taken as a reference run for the Pb–Pb data taking in 2010. For the analysis an offline event selection has been applied to reject events, which do not fulfill the central barrel trigger conditions or which are not of physics type (e.g. calibrations events). Furthermore, events assigned to noise or beam-gas interactions were rejected. This selection is called *Physics Selection* (PS). In this period several triggers were running, but only events which are consistent with the minimum bias trigger (MB_{OR}) are taken into account. This trigger requires a hit in either SPD or one of the two V0 detector (VZERO) detectors. This trigger allows to investigate a nearly unbiased sample of collisions, just aiming at not recording empty event, which could occur due to the limited acceptance of ALICE.

3.2.1 Event Selection in pp Collisions

In addition to the criteria mentioned above, the events selected in the analysis have to have a reconstructed primary vertex with $|z_{vtx}| < 10$ cm to the center of ALICE. This vertex can be reconstructed either with global tracks or only SPD tracklets. However, it has to have at least one contributing track or tracklet to the vertex.
For the data taken in the LHC11a period, with the latest reconstruction pass (so called "pass 4“) the number of collected events is $\sim 33.8 \cdot 10^6$ and approximately $26.6 \cdot 10^6$ events survive the afore mentioned selection criteria.
It has been found that the primary vertex finding efficiency is not 100%, but $\epsilon_{\text{Vtx}}^{\text{SPD}} = 91\%$ which we need to take into account in order to arrive at the final of events for the normalization.
The spectra are normalized with the following number of events:

$$N_{\text{evt}}^{\text{MB}} = N_{\text{evt}}^{\text{ana}} \frac{1}{\epsilon_{\text{Vtx}}^{\text{SPD}}} (1 - f_{\text{PU, bunch}})(1 - f_{\text{PU, train}}). \tag{3.3}$$

Where $f_{\text{PU, bunch}}$ and $f_{\text{PU, train}}$ are the probabilities of pileup from the same bunch crossing and consecutive bunches, respectively. As any bunch crossing has some probability to produce an event, there is the possibility that two (or more) collisions happen at the “same” time and are recorded as one event. During the 2011 LHC11a data-taking period, the beam bunches were grouped into 9 *trains*, each train containing 8 bunches or *wagons*[1].[30] Figure 3.2 attempts to visually summarize the beam conditions/parameters. Since the signal integration window for the EMCal is 200 ns, intra-train pile-up is not an issue with a 525 ns wagon spacing. Figure 3.3 shows the cluster time vs energy distribution. The only timing peak is centered at $t = 0$, illustrating that the EMCal was not sensitive to pile-up from subsequent wagons. However, there is always the probability that two (or more) collisions can occur *within a single bunch crossing*. For the estimation of intra-bunch pile-up, the cluster timing distribution for the PHOS detector is shown in Figure 3.4 as the blue curve. The red curve along with the orange and blue histograms are derived via a Toy MC whose only input are the beam/bunch parameters taken from [30] and shown in Figure 3.2. The complex shape is completely understood as a combination of intra-train and intra-bunch pile-up.
The peaks of Figure 3.4 can be integrated and their ratios used to determine the Poisson probability, μ, for *exactly k collisions* to occur in a given bunch crossing

[1]Technically, there are 13 trains but the first 4 are single-wagon trains and not even steered to collide at Point 2

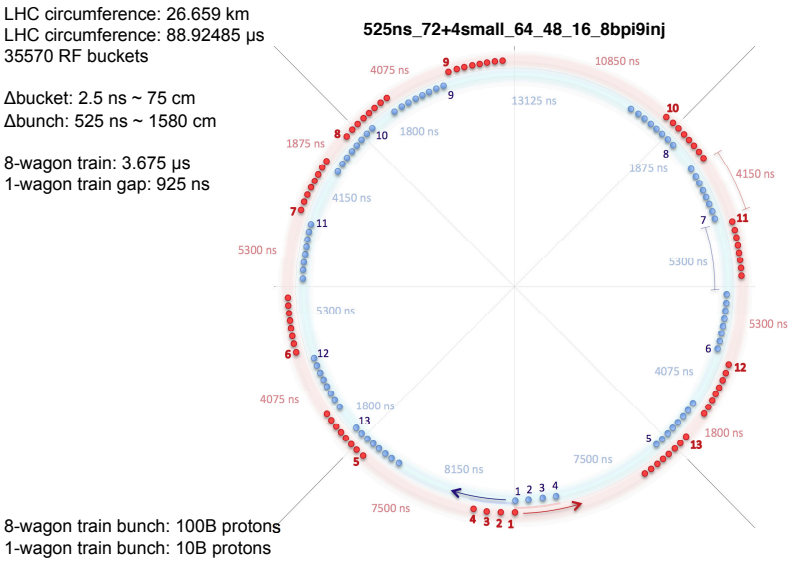

Figure 3.2: Injection scheme for LHC11a.

(taking into account finite train lengths). The parameter μ was calculated to be roughly 4%. This is in agreement with estimations made with the SPD for the probability for *exactly 2 collisions* to occur in a single bunch crossing to be $\sim 1.9\%$. While it may be surprising that the probability for intra-bunch pile-up is half as likely as intra-train pile-up, it is a natural consequence of Poisson statistics in the limit that the mean $\mu \ll 1$. The probability for k collisions to occur with a mean, μ, is

$$\mathrm{P}(k;\mu) = \frac{\mu^k e^{-\mu}}{k!} \tag{3.4}$$

and the probability for *at least 1 or more* collisions to happen in a given bunch crossing is

$$\mathrm{P}_{\text{any}}(\mu) = \sum_{k=1}^{\infty} \frac{\mu^k e^{-\mu}}{k!} = e^{-\mu}\left(\mu + \frac{\mu^2}{2} + \frac{\mu^3}{6} + ...\right) \tag{3.5}$$

which for $\mu \ll 1$ can be approximated by

$$\mathrm{P}_{\text{any}}(\mu) \approx e^{-\mu}\left(\mu + \frac{\mu^2}{2}\right) \tag{3.6}$$

Now, since it is required that there was at least 1 minimum bias event occuring (otherwise the trigger would not fire), the probability to have 2 collisions occur under this conditional probability is

$$\mathrm{P}_{MB\ trig}(2;\mu) = \frac{\mathrm{P}(2;\mu)}{\mathrm{P}_{\text{any}}(\mu)} \approx \frac{\frac{\mu^2 e^{-\mu}}{2}}{e^{-\mu}\left(\mu + \frac{\mu^2}{2}\right)} = \frac{\mu^2/2}{\mu + \mu^2/2} \tag{3.7}$$

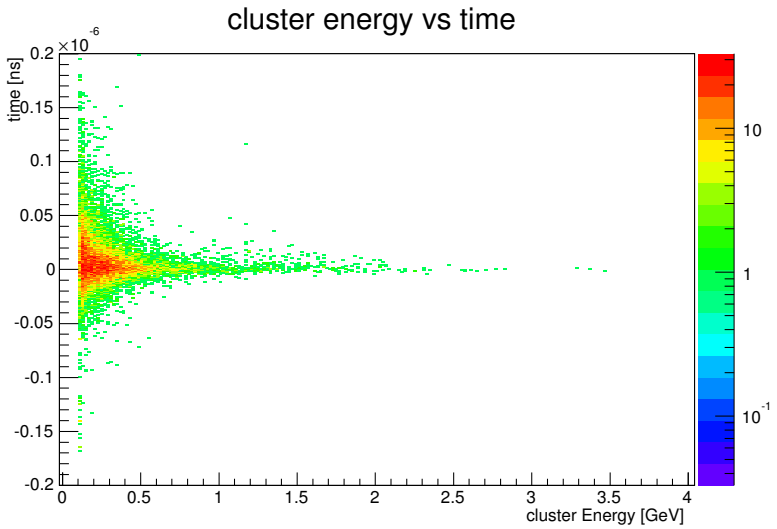

Figure 3.3: Time of the clusters being registered versus energy deposited in the EMCal by the photon candidate for pp collisions at $\sqrt{s} = 2.76$ TeV taken in the beginning of 2011.

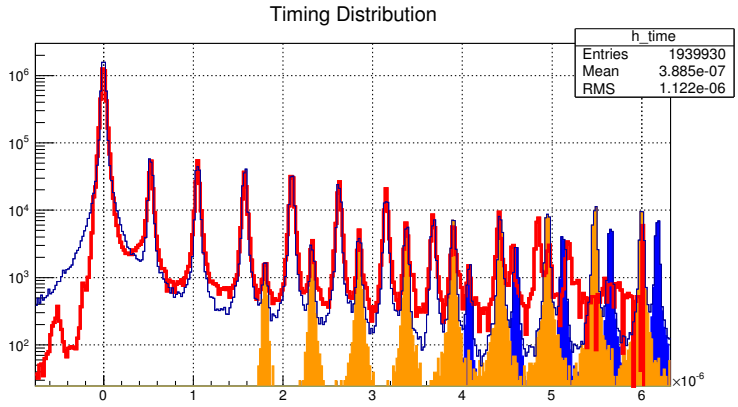

Figure 3.4: The PHOS timing distribution is shown as the blue curve. The red curve is the distribution derived via a Toy MC using only the beam parameters as input. The orange and blue histograms illustrate peaks coming from subsequent *trains*. Specifically, the orange results from trains that have ~ 1.8 μs spacing which the blue results from trains that have ~ 4.1 μs spacing.

Again, since $\mu \ll 1$, the term in the denominator can be approximated as

$$\mu + \frac{\mu^2}{2} \approx \mu \tag{3.8}$$

therefore making Equation 3.7

$$\mathrm{P}_{MB\ trig}(2;\mu) \approx \frac{\mu^2/2}{\mu} = \frac{\mu}{2} \tag{3.9}$$

The probability for 2 collisions to occur in a given bunch crossing, once we've already assumed that the minimum bias trigger fired is $\mu/2$, whereas the probability for a

collision to happen in a subsequent bunch crossing (we don't require a MB trigger to have fired on the subsequent bunch crossing) is $\mu e^{-\mu}$, which for $\mu \ll 1$ is simply μ.
The final yield is therefore scaled by 0.98 to remove this intra-bunch pile-up.

3.2.2 Monte Carlo Simulations

In order to obtain efficiency and acceptance corrections in pp collisions two different Monte Carlo event generators are used as input for our full detector simulation: **Phojet** [31, 32] and **Pythia 8.1** [33, 34]. Both generators are general purpose event generators.

Pythia 8

Pythia 8 is an event generator, which is designed to reproduce the high momentum physics accessible at the LHC, thus the event generation in Pythia starts with the simulation of the hard scattering process, taking by default the description of the initial states from the CTEQ 5L parton density functionss (PDFs) [35] and is optimized for leading order $2 \longrightarrow 1$ and $2 \longrightarrow 2$ processes.
However, in order to reproduce the measured data, also diffractive processes based on Regge Field Theory [36] were implemented. Compared to previous versions it is possible import process level events via the Les Houches Accord (LHA) and Les Houches Event Files (LHEF), thus the need to implement an extensive process library in Pythia itself has decreased. Therefore, the focus for Pythia 8 has shifted to a good description of the subsequent steps, such as initial- and final state parton showers, multiple parton-parton interaction, string fragmentation and decay. The initial- and final-state algorithms are based on a $p_\perp$-ordered evolution, which was introduced in Pythia 6.3. The hadronization simulations are based on the LUND String Model [37].
The full particle decay tables are taken from [38] and implemented in the framework and the hadrons are decayed accordingly. As Pythia combines a lot of different processes, it has many tunable parameters with significant influence on the generated distributions, reflected especially in the low momentum transfer processes. One of these parameters is the connection between low and high momentum processes, which is given by a minimum momentum transfer ($p_{T,\text{cut-off}}$) of 2 GeV/c.

Phojet

This Monte Carlo event generator uses ideas of the Dual Parton Model (DPM) [39], dominant in the soft scattering regime, combined with perturbative QCD, dominant in the hard scattering regime, to give an almost complete picture of hadron-hadron, photon-hadron and photon-photon interactions at high energies [32]. With the Dual Parton Model it is possible to simultaneously calculate the elastic (i.e cross sections) and inelastic processes (i.e. multiparticle productions) within a single event. Therefore, the model directly relates the free parameters necessary to describe the cross sections to the multiparticle production. As in Pythia the parton showers are initiated following the DGLAP evolution equations [40] and the hadronization is based on the LUND fragmentation model. Furthermore, the same decay table are used to produce decay the hadrons.
The soft and hard part of the interaction are separated by a $p_{T,\text{cut-off}}$ of 3 GeV/c. However, within the two-component DPM the connection of the soft and hard subprocesses is given by an unitarization scheme, chosen in a way that the sum of the hard and soft cross sections is nearly independent of the $p_{T,\text{cut-off}}$. Therefore, the tune parameters, unlike for Pythia, are connected to each other.

Both Monte Carlo event generators fail to fully reproduce the transverse momentum spectrum of the neutral pion and photons in general with the same tune at low and high transverse momentum simultaneously. Thus the average of both Monte Carlo generators is taken for the efficiency and acceptance corrections. The remaining discrepancy between the Monte Carlo generators is taken as a systematic error source, however, this discrepancy for pp collisions at $\sqrt{s} = 2.76$ TeV is smaller than 2.5% for the photons and therefore negligible compared to the other systematic uncertainties.
The Monte Carlo samples used were generated anchored to the full accepted run list of the LHC11a data set, thus they should reproduce the detector conditions nearly perfectly. Two samples were used for the corrections in this thesis:

LHC12f1a
This Monte Carlo data set is based on Pythia 8 as event generator. Approximately $37.7 \cdot 10^6$ events were generated.

LHC12f1b
Using Phojet as event generator this Monte Carlo sample provides approximately $37.5 \cdot 10^6$ events.

The GEANT3 [41] description of the ALICE detector takes the input distributions from the afore mentioned generators as input and then simulates ALICE detector response to them. The resulting output is then run through the reconstruction software which generates output in a similar format to the actual data (although the final output files also contain the "input particle" information as well).

3.3 Photon Candidate Selection and Calibration

In an electromagnetic calorimeter like the EMCal not only photons leave a signal. Other hadrons and particularly leptons will leave a signature as well. Most of these signals will be shaped differently however. Thus allowing us to distinguish at least between the energy deposit of charged hadrons and electromagnetic probes. To obtain a fairly clean sample of photon and electron candidates, the V2 clusterizer was ran with a seeding threshold of 300 MeV and only cells with a minimum energy of 50 MeV were associated to such clusters. Furthermore a preselection and calibration was run on the possible clusters, which rejected the energy deposit in noisy or dead channels and removed very high energetic nearly single cell clusters, which most likely stem from neutrons interacting directly with the electronics of the EMCal.
Additionally clusters with only 1 contributing cell were rejected and a minimum energy deposit in the cluster of 400 MeV total was required.

3.3.1 Calibration Procedure

A basic calibration on the cell-by-cell level is done in the central framework of ALICE in order to correct for cluster timing variations due to different readout cable lengths and offsets and the inaccuracies of the readout in converting the energy deposit into digital signals. In addition to that a temperature calibration on a run-by-run level has been performed in the same framework.
In order to correct the final neutral pion spectrum we need to ascertain the absolute calibration of the energy deposit in the data however. This is normally done by generating Monte Carlo simulations of the detector response using the description in GEANT3 [41] or GEANT4 [42] and the respective event generators as input for the physics quantities and comparing those distributions to the ones observed in the data.
In princple, the GEANT simulation should describe the detector response in totality. However, this premise must not be taken for granted. The calibration between data

and MC must be properly accounted for in order to trust that the MC is accurately describing the EMCal. The traditional strategy to ensure that the MC response matches the data is to independently calibrate both the data and the Monte Carlos simulation. In the simulation, one can compare the input energy of a given photon to the simulated detector response of the EMCal. Figure 3.5 shows the uncorrected ratio of the input energy, E_{truth}, to the reconstructed cluster energy, E_{rec}, as a function of E_{rec}.

The left panel of Figure 3.6 shows the uncorrected ratio of E_{truth}/E_{rec}, fit in energy

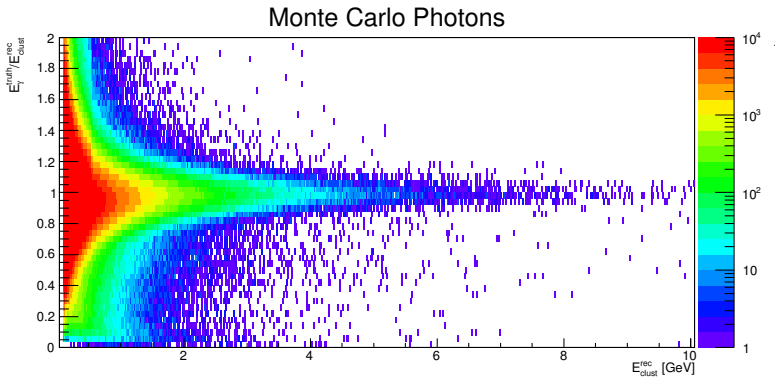

Figure 3.5: E_{truth}/E_{rec} vs E_{rec}.

slices as a function of E_{rec}. The officially obtained correction function, $kPi0MCv3$, is overlaid in red. Since this is a correction to the cluster energy *as a function of the cluster energy*, this is referred to as a "non-linearity" correction. After applying

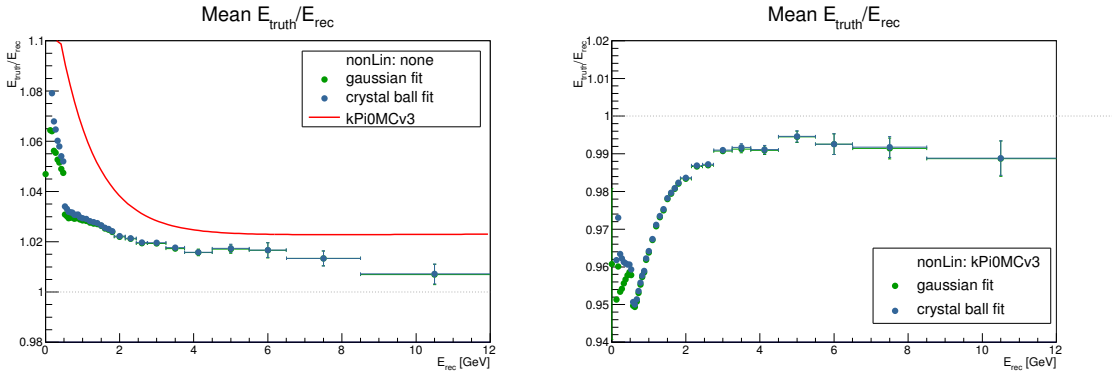

Figure 3.6: The fit mean E_{truth}/E_{rec} vs E_{rec} without any non-linearity correction applied (left panel) and after applying $kPi0MCv3$ as a non-linearity correction (right panel).

the non-linearity correction $kPi0MCv3$, one hopes that the ratio of E_{truth}/E_{rec} is roughly flat at 1. The non-linearity corrected ratio is plotted in the right panel of Figure 3.6. While the divergence from unity is expected due to the mismatch

of the function $kPi0MCv3$ in the left panel, this is not the desired outcome of the non-linearity correction and stems from the usage of simulations which were done without additional material in front of the calorimeter. Meaning the function $kPi0MCv3$ would account for the real detector response, while in a full detector simulation of ALICE the photons might convert in one of the lower detectors and thus the detector response will have to incorporate for energy loss due to conversions as well.
In order to obtain the simple correction factors for the response of the calorimeter in reality as well, test beam information can be used. For this purpose during the testing and commissioning of the EMCal, some of the detector modules were put in front of a beam of electrons (with a known energy) and the response was measured. A procedure similar to what is described above for MC is then employed for the test beam data. The resulting non-linearity correction is called $kBeamTestCorrectedv2$. This correction as already mentioned cannot account for the loss of energy due to conversions in the material of for instance the TRD or TOF.
The functional forms used for the two corrections is listed below.

$$f(x) = \frac{p_6}{p_0}\left[\frac{1}{1+p_1\cdot e^{\frac{-x}{p_2}}}\cdot\frac{1}{1+p_3\cdot e^{\frac{x-p_4}{p_5}}}\right] \tag{3.10}$$

Of course, p_0 and p_6 in this equation are directly inversely correlated and in future fits, p_0 should be fixed to 1.

Symmetric Decay Method (SDM)
In order to fully correct the shift in the energy in the full detector setup a method exploiting symmetric π^0 decays has been developed, where the asymmetry of the decay is defined as

$$\alpha(p_{\gamma_1}, p_{\gamma_2}) = \frac{|p_{\gamma_1} - p_{\gamma_2}|}{p_{\gamma_1} + p_{\gamma_2}} \tag{3.11}$$

In the rest frame of the π^0, a symmetric photon pair ($asymmetry \sim 0$) is one whose decay axis is perpendicular to the π^0's momentum in the lab frame. In contrast, an asymmetric decay ($\alpha \sim 1$) is one in which the decay axis is parallel to the π^0's momentum. In order to obtain the new correction function a strict cut on the asymmetry $\alpha < 0.1$ of the two photons is used. Thus allowing to assume that the energy of the two photons is approximately the same, which simplifies the invariant

mass of the π^0 to

$$\begin{aligned} m^2_{\pi^0} &= 2E_{\gamma_1}E_{\gamma_2}(1-\cos\theta) \\ &\approx 2E^2_{\gamma}(1-\cos\theta) \end{aligned} \tag{3.12}$$

The invariant mass distribution measured in the data is then shifted by Equation 3.13 in order to shift the neutral pion peaks to the position observed in the Monte Carlos simulations.

$$f(p_T^{\pi^0}) = p_0 + e^{p_1+p_2 p_T^{\pi^0}}, \tag{3.13}$$

Here p_0, p_1, and p_2 are free parameters. The functional form is derived empirically and is thus not based on any basic physics principles. Afterwards the ratio of data and Monte Carlo is fitted and the non-linearity correction for the clusters in the data can be calculated as

$$f(2E_\gamma) = p_0 + e^{p_1+p_2\cdot(2E_\gamma)} \tag{3.14}$$

under the assumption that $p_T^{\pi^0} \approx E^{\pi^0} \approx 2E^{\gamma}$.
Of course, within the analysis, any non-linearity correction to the data must have a corresponding non-linearity correction to the MC. To obtain the needed correction in MC, we look to the ratio of E_{truth}/E_{rec} as a function of E_{rec} for different categories of clusters. By separating the sample into 4 types of clusters, the apparent detector response can be better understood. Figure 3.7 describes and illustrates these categories. The left panel of Figure 3.8 shows the detector response to three

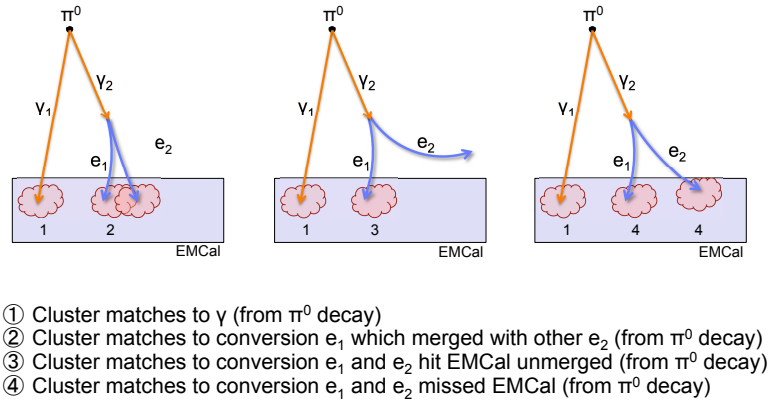

Figure 3.7: Definitions of different cluster categories from MC truth information.

of these categories as well as to all clusters. All clusters considered are identified

as a π^0 decay product. In addition, $kPi0MCv3$ is plotted as a dashed line. Using the functional form of $kPi0MCv3$, the data are fit for the inclusive clusters (that pass the cuts). Since the p_{T} of this MC sample is limited, in this fit with Equation 3.10, we fix $p_0 = 1$ and the high momentum parameters, $p_{3,4,5}$, to the values found from $kPi0MCv3$. The resulting values for for the remaining 3 parameters are: $p_1 = 0.0665$, $p_2 = 1.570$, and $p_3 = 0.0968$. This parameterization of of Equation 3.10 is the non-linearity correction that is applied to the MC and is called $kPi0MCv5$. The right panel of Figure 3.8 shows the response of all π^0 decay product clusters af-

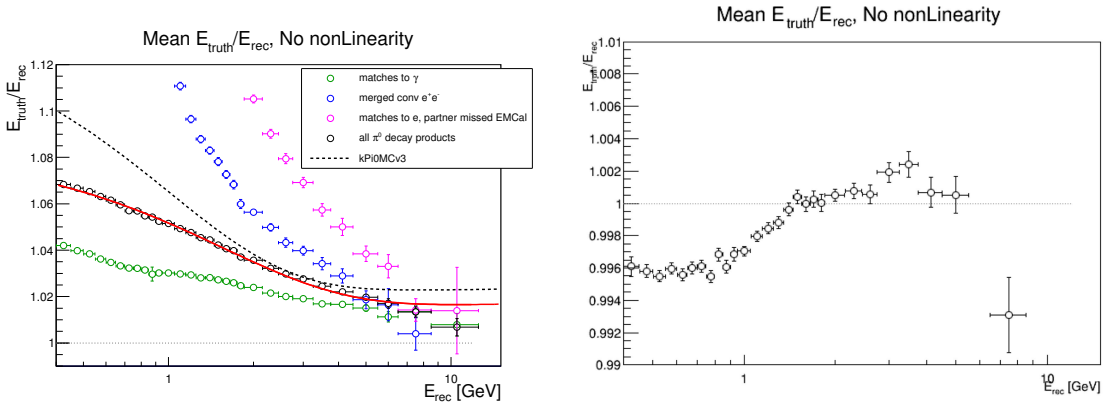

Figure 3.8: Ratio of truth energy to mean reconstructed energy for cluster associated with a π^0 decay before non-linearity correction (left) and after $kPi0MCv5$ (right). The $kPi0MCv5$ fit is shown as the red curve in the left panel.

ter applying $kPi0MCv5$. The residual energy mismatch is within 0.5% of the truth and only significantly deviates from unity below $\sim$ 1.5 GeV of the reconstructed cluster.

The full procedure is afterwards applied to the data and Monte Carlo simulation and the correction factors are calculated as

$$\text{data: } E^{\text{new}}_{\text{cluster}}(E^{\text{old}}_{\text{cluster}}) = kPi0MCv5(E^{\text{old}}_{\text{cluster}}) \cdot kSDM(2.0 \cdot E^{\text{old}}_{\text{cluster}}) \quad (3.15)$$

$$\equiv kSDMv5(E^{\text{old}}_{\text{cluster}}) \quad (3.16)$$

$$\text{MC: } E^{\text{new}}_{\text{cluster}}(E^{\text{old}}_{\text{cluster}}) = kPi0MCv5(E^{\text{old}}_{\text{cluster}}) \quad (3.17)$$

Where the function $kSDM$ is defined as:

$$kSDM(2.0 \cdot E_{cluster}) = p_0 + e^{p_1 + p_2 \cdot 2.0 \cdot E_{cluster}} \quad (3.18)$$

with $p_0 = 0.964$, $p_0 = -3.132$, and $p_0 = -0.435$. Essentially by construction, after applying these corrections, the mass positions should match in data and MC if the same asymmetry cut is applied. The full efficiency of the procedure is truly tested

in the simultaneous comparison of the π^0 and η peak positions and widths, which will be shown in Section 3.5.

A similar procedure can then be applied to the test beam data and a new set of parameterizations is found $kSDMv6$ and $kPi0MCv6$.

In this thesis the standard non-linearity correction used is the more sophisticated SDM method based on real collision data (kSDMv5) and the corresponding Monte Carlo correction. The two set of parameters obtained using the test beam data will be used for systematic error calculations nonetheless.

A summary plot of all the functional for in the representation of the test beam data compared to the test beam data and the Monte Carlo simulations can be seen in Figure 3.9.

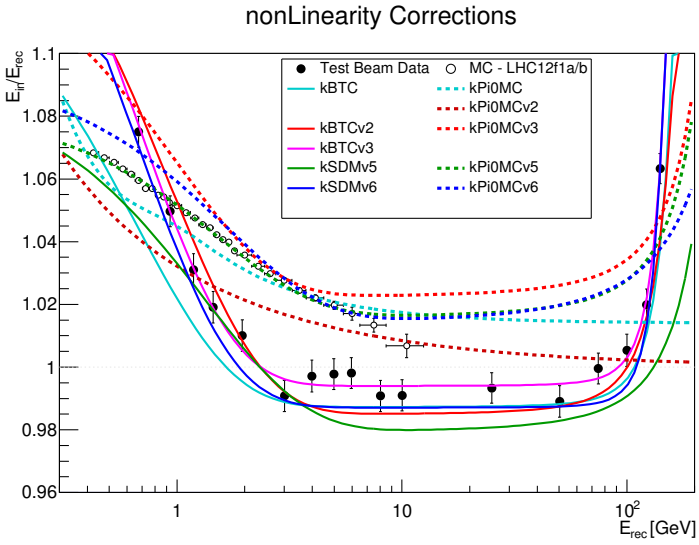

Figure 3.9: All of the available non-linearity corrections overlaid.

3.4 Neutral Pion Signal Extraction

After having selected the good photon candidates, they are paired and the invariant mass is calculated. As already described all pairs are calculated, leading to a significant combinatorial background which needs to be estimated and subtracted in order to extract the signal yield.

In order to reproduce the pure combinatorial background photons from different events are combined in a so-called mixed event background estimate. This is done in bins of charged particle multiplicity, primary vertex position in beam direction

and transverse momentum. Using this technique the statistical uncertainties on the background estimate can be reduced, by mixing a large number of photons from different events i.e. 80. Additionally the systematic uncertainties from the background subtraction are reduced at the same time, due to the knowledge of the actual uncorrelated background compared to simple side-band fitting method with polynomial of order n. However, in this estimate one source of background is neglected in this estimate, the correlated background arising from jet in the event.
Traditional background subtraction methods typically involve arbitrary mass dependent scaling functions that assume no knowledge of the actual background shape. These arbitrary functions are applied to the mixed event distribution and then subtracted from the raw spectrum in order to cure the mismatch between the background shape in the actual raw distribution and the mixed event distribution. Within this thesis however an attempt is made to disentangle multiple sources of background and apply that knowledge to the overall background estimation. Rather than assuming

$$TotalBackground = N \cdot f(p_{T,\pi^0}) \cdot Combinatorial \tag{3.19}$$

where N is an overall normalization constant and $f(p_T)$ is the mass dependent scaling function and $Combinatorial$ is the combinatorial background derived via mixed events, the background estimation in this analysis is constructed as

$$\begin{aligned} TotalBackground &= N_1 \cdot Combinatorial + CorrelatedBackground \\ &= N_1 \cdot Combinatorial + N_2 \cdot JetBkg \end{aligned} \tag{3.20}$$

By injecting assumptions about the physics of correlated background, the need for arbitrary fitting is diminished. Not only can this reduce the systematic uncertainty associated with the background estimation but it can also allow the measurement to begin to probe low $p_{\mathrm{T}}\pi^0$s where the signal-to-background drops below $10-15\%$. A fast Monte Carlo is used to generate the estimated correlated background. This toy Monte Carlo draws from the two dimensional delta phi versus transverse momentum for charged hadrons two random directions and transverse momenta and combines those asuming they would be photons into an invariant mass and transverse momentum of the pair. This exercise can be repeated until the statistics for the correlated background seems suffiencient.
Since the mixed events and correlated background have arbitrarily large statistics,

they must both be normalized before subtraction. A fit is performed to the data simultaneously in $50 < m_{\gamma\gamma} < 80$ MeV/c^2 and $200 < m_{\gamma\gamma} < 250$ MeV/c^2 with the normalizations of the mixed events and correlated background being the only free parameters. The *shapes* of the backgrounds are held fixed. The results of this procedure for $1.8 < p_{\mathrm{T}} < 2.0$ GeV/c are shown in Figure 3.10. For reference, all of the p_{T} bins are plotted in the Appendix in Section 6.1. The background is extremely well estimated using this method.

Once the background has been subtracted, the raw yield must be extracted from

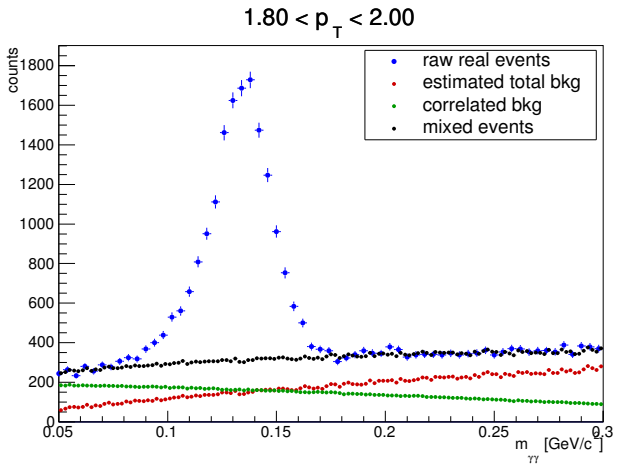

Figure 3.10: The background estimation for $1.8 < p_T < 2.0$ GeV/c.

the remaining pion peak. There are four extraction procedures performed. Three fitting functions and a counting method. The functions used are

- Gaussian

$$f(m) = N\, e^{-\frac{(m-\mu)^2}{2\sigma^2}} \tag{3.21}$$

having 3 free parameters: μ is the mean of the peak, σ is the width, and N is the normalization.

- Asymmetric Gaussian

$$\begin{aligned} \text{for } \; m < \mu\text{:} \quad & f(m) = N\, e^{-\frac{(m-\mu)^2}{2\sigma_1^2}} \\ \text{for } \; m \geq \mu\text{:} \quad & f(m) = N\, e^{-\frac{(m-\mu)^2}{2\sigma_2^2}} \end{aligned} \tag{3.22}$$

having 4 free parameters: μ is the mean of the peak, σ_1 is the width on the low mass side, σ_s is the width on the high mass side, and N is the normalization.

- Crystal Ball

$$\text{for } \frac{m-\mu}{\sigma} > -\alpha: \quad f(m) = N\, e^{-\frac{(m-\mu)^2}{2\sigma^2}}$$
$$\text{for } \frac{m-\mu}{\sigma} \leq -\alpha: \quad f(m) = N \cdot \left[\frac{n}{|\alpha|} - |\alpha| - \frac{m-\mu}{\sigma}\right] \cdot \left(\frac{n}{|\alpha|}\right)^n \cdot e^{-\frac{|\alpha|^2}{2}} \tag{3.23}$$

having 5 free parameters: μ is the mean of the peak, σ is the width, and N is the normalization. The Crystal Ball shape is a Gaussian that is connected to an exponential tail at 'α' sigma of the Gaussian. The sign determines if it happens on the low mass side or high mass side. The n parameter controls the slope of the exponential. The Crystal Ball function is frequently used to model energy loss of decay products and thus typically aims to describe a low mass tail.

The counting method simply counts the yield within $\pm 3.5\sigma$ of the mean found with the Gaussian fit. The estimated π^0 signal is plotted in Figure 3.11 along with the various fit functions. To account for any residual background, the functions are fit with a straight line ("pol1") baseline. In the counting method, the same pol1 residual background is subtracted before counting to ensure that any systematically negative bins aren't artificially reducing the yield. There is a systematic difference in the ex-

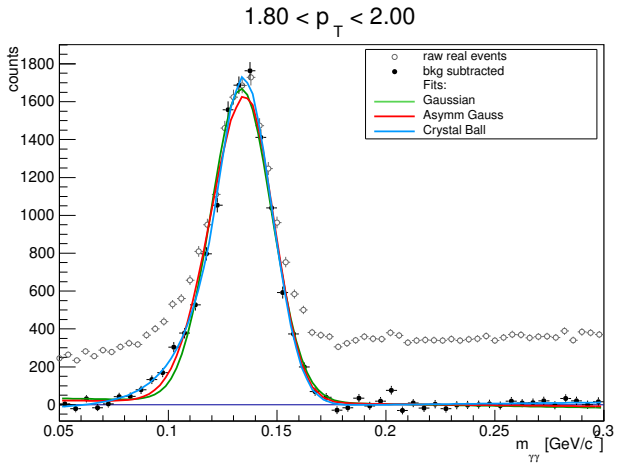

Figure 3.11: The signal extraction for $1.8 < p_T < 2.0$ GeV/c.

tracted π^0 peak positions for the different fitting functions. To see the overall trend, refer to Section 6.2. For reference, in the p_{T} bin shown ($1.8 < p_T < 2.0$ GeV/c) the extracted means and sigmas are

- Gaussian:
  $\mu = 133.6 \pm 0.2$ MeV/c^2 and $\sigma = 14.0 \pm 0.2$ MeV/c^2

- Asymmetric Gaussian:
  $\mu = 135.7 \pm 0.3$ MeV/c^2, $\sigma_{low} = 16.2 \pm 0.4$ and $\sigma_{high} = 12.6 \pm 0.1$ MeV/c^2

- Crystal Ball:
  $\mu = 134.6 \pm 0.2$ MeV/c^2 and $\sigma = 12.8 \pm 0.2$ MeV/c^2

3.5 π^0 and η Mass Peak Position and Resolution

In order to judge whether the Monte Carlo simulations after the calibrations can be used for the corrections the same fitting procedure as described in Section 3.4 is performed on the reconstructed Monte Carlo data in the same momentum slices as for the data. Any mismatch in the fitted mass positions directly translates to a mismeasurement in the momentum of the measured π^0, highlighted by the following relation:

$$\begin{aligned} m^2_{\pi^0} &= (\mathbf{P}_{\gamma_1} + \mathbf{P}_{\gamma_2})^2 \\ &= (E_{\gamma_1} + E_{\gamma_2})^2 - (\vec{p}_{\gamma_1} + \vec{p}_{\gamma_2})^2 \\ &= (|p_{\gamma_1}| + |p_{\gamma_2}|)^2 - (|p_{\gamma_1}|^2 + |p_{\gamma_2}|^2 + 2p_{\gamma_1}p_{\gamma_2}\cos\theta) \\ &= |p_{\gamma_1}|^2 + |p_{\gamma_2}|^2 + 2p_{\gamma_1}p_{\gamma_2} - |p_{\gamma_1}|^2 - |p_{\gamma_2}|^2 - 2p_{\gamma_1}p_{\gamma_2}\cos\theta \\ &= 2p_{\gamma_1}p_{\gamma_2} - 2p_{\gamma_1}p_{\gamma_2}\cos\theta \\ &= 2p_{\gamma_1}p_{\gamma_2}(1 - \cos\theta) \end{aligned} \tag{3.24}$$

Since the $m^2_{\pi^0}$ is proportional to the product of the two photon's momenta (p_{γ_1} and p_{γ_2}), any discrepancy in the reconstruction of the mass position will also manifest in a misreconstruction of the π^0's momentum:

$$p^2_{T,\pi^0} = (p_{x,\gamma_1} + p_{x,\gamma_2})^2 + (p_{y,\gamma_1} + p_{y,\gamma_2})^2. \tag{3.25}$$

A toy Monte Carlo has been written to test the dependence of the yield on the overall energy scale calibration. Using a "realistic" π^0 input p_{T} distribution (obtained from the 2.76 GeV published π^0 invariant cross section measurement [1]), π^0 were thrown and (naively) decayed symmetrically to $\gamma\gamma$. The decay photons' energies

were then scaled by a miscalibration factor and the miscalibrated π^0 momentum was recalculated. The ratio of the miscalibrated π^0 momentum to the "real" thrown momentum is plotted in Figure 3.12. Since the pion has an intrinsic steeply falling momentum spectrum, shifting the π^0's p_{T} by 2% corresponds to an approximate shift in the overall measured yield of $\sim 7-8\%$. The flat-line fits to the ratios are: $1\% \sim 0.963$, $2\% \sim 0.928$, $3\% \sim 0.893$ in the range of $1-18$ GeV/c.

While the π^0 mass peak is (relatively) easy to identify from the background, any

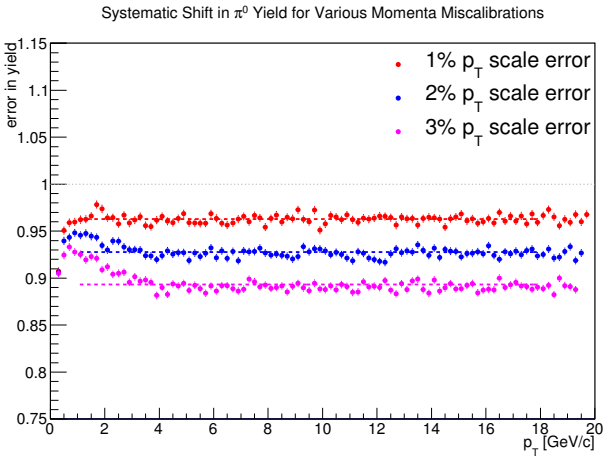

Figure 3.12: Using a Toy MC with a "realistic" input p_{T} distribution, the various shifts in the overall yield were estimated. Flat line fits were performed from $1-18$ GeV/c.

systematic shift in the mean reconstructed position must be reproduced in the Monte Carlo to ensure an accurate final p_{T} spectrum. In order to see the effects of the new SDM calibration procedure for the clusters the fitted mass postion and width for the neutral pions and η mesons are compared between data and Monte Carlo for each uncorrected (Figure 3.13) and corrected clusters (Figure 3.15).

The mass for each particle is represented as the mean of a gaussian fit to the diphoton distribution after background subtraction divided by the PDG value of the meson's mass. The ratio of MC/data of the π^0 for the uncorrected clusters shows that above ~ 2 GeV/c, the MC and data differ by roughly a constant scale factor of ~ 0.981 while for the η the factor is ~ 0.972.

The η meson is a powerful cross check to the pion mass position and width. Unfortunately, since there are far fewer ηs than $\pi^0 s$, the η is more sensitive to the combinatorial background. With the statistics of the LHC11a dataset, the η is unresolvable below about $p_{\mathrm{T}} < 1.5$ GeV/c. However, above this p_{T}, the η serves as a (low statistics) verification of the energy calibrations. The $\sim 2\%$ difference between the MC/data ratio of the π^0 and η mass positions suggests that there is some fun-

damental need for a nonLinearity correction.

The π^0 mass position is also dependent on the photon cuts made on the clusters.

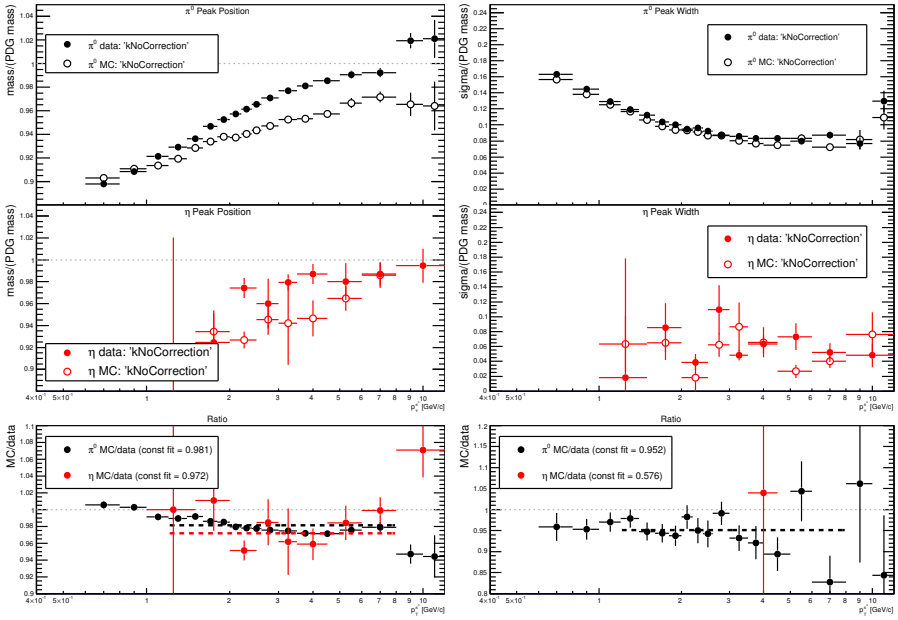

Figure 3.13: The mean mass position (left panel) and peak width (right panel) vs pT without applying any nonLinearity correction for the π^0 (top row) and η mesons (middle row). The masses are normalized by the PDG values. Both data and MC are plotted and the ratio of MC/data is shown in the bottom row.

Using a more restrictive set of cuts in Figure 3.14 (namely applying a shower shape cut on the λ_0^2 variable as well as raising the cluster's E_{min} from 100 MeV to 300 MeV) the ratio becomes even flatter (at ~ 0.984) while still consistent with Figure 3.13. The primary reason is that the λ_0^2 cut removes late conversions from the sample so that we are measuring mostly photons in the calorimeter. However, these late conversions don't hurt us; on the contrary, we can use them to increase the π^0 signal as the e^+ and e^- cluster showers typically merge and simply shift the π^0 mass peak to *slightly* lower values ($\sim$1-2%).

If the SDM corrections ($kPi0MCv5$ and $kSDMv5$) are used, however, (Figure 3.15) the agreement between data and Monte Carlo is striking. Both the π^0 and η are simultaneously within 0.5%. Additionally, the widths are also reasonably well described. The width is more delicate still, since we are using a gaussian fit to a distribution that is inherently (slightly) asymmetric. Nevertheless, the width of the peak is mostly important for the integration windows for the yield extraction. Therefore, the extracted yield is inherently less sensitive to the width than the peak position. To determine the optimal non-linearity correction the same exercise was

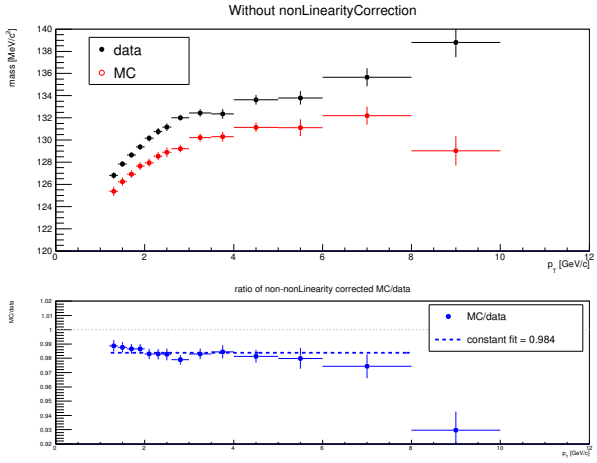

Figure 3.14: The mean mass position vs pT without applying any nonLinearity correction. Here a shower shape cut is made on the variable $M02$ as well as E_{min} of the cluster being greater than 300 MeV

performed for the two other non-linearity correction which are anchored to the test beam data. It was found that the agreement for the pure testbeam data driven corrections ($kBeamTestCorrectedv2$ and $kPi0MCv3$) mismatches by approximately 1%(2%) for the π^0 and η, respectively. While the $kSDMv6$ and $kPi0MCv6$ lead to a mismatch of approximately 0.2% for both particles. Thus it was decided to use the $kSDMv5$ and $kPi0MCv5$ as standard corrections and the remaining variations for a systematic error estimate.

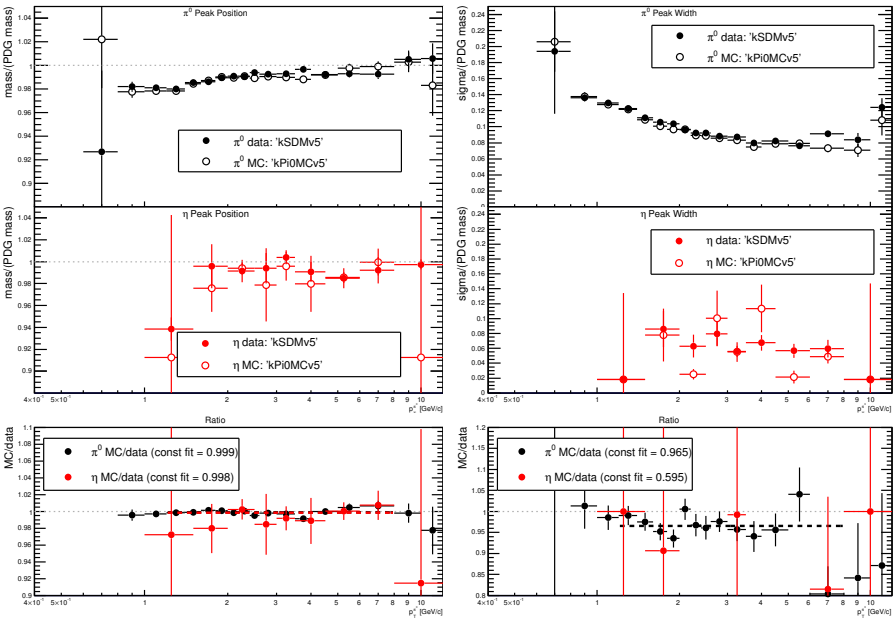

Figure 3.15: The mass position (left panel) and the peak width (right panel) vs pT with non-Linearity corrections applied for the π^0 (top row) and η mesons (middle row). The masses are normalized by the PDG values. The data uses $kSDMv5$ while the Monte Carlo uses $kPi0MCv5$. The ratio of MC/data is shown in the bottom row.

3.6 Neutral Pion Correction Procedure

In order to arrive to the final spectra, after having obtained the raw yield of the mesons, several corrections need to be applied. At first corrections for the geometrical acceptance and reconstruction efficiency are applied. Afterwards, the contribution from secondary π^0 mesons from weak decays or hadronic interactions in the detector material need to be removed from the reconstructed neutral pions yield to allow us to compare the measurement to existing theory calculations. In addition to that the spectra are corrected for the finite bin width in transverse momentum.

3.6.1 Efficiency and Acceptance Correction

Any experimental setup and apparatus suffers from inefficiencies. However, detailed Monte Carlo simulations provide the ability to correct for these detector deficiencies and measure final particle yields (with some degree of uncertainty). Both the reconstruction efficiency and correction due to the limited acceptance are calculated and applied.
While the factorization of the acceptance and efficiency is an often debated line-in-the-sand, we define two sets of acceptance and reconstruction efficiency: the *pure* $\{\varepsilon_{rec}^{pure}, \varepsilon_{acc}^{pure}\}$ and the *effective* $\{\varepsilon_{rec}^{eff}, \varepsilon_{acc}^{eff}\}$. In the case of the *effective* acceptance this essentially condenses to a constant factor with respect to p_{T}. The reciprical of the product of each is equal to the total correction applied to the data.

Pure ε_{rec} and ε_{acc}

$$\varepsilon_{rec}^{pure} = \frac{reconstructed\ \&\ extracted\ \pi^0}{\pi^0(1.40 < \phi_{\gamma_{1,2}} < 3.15\ \&\&\ |\eta_{\gamma_{1,2}}| < 0.65)} \tag{3.26}$$

$$\varepsilon_{acc}^{pure} = \frac{\pi^0(1.40 < \phi_{\gamma_{1,2}} < 3.15\ \&\&\ |\eta_{\gamma_{1,2}}| < 0.65)}{\pi^0(0 < \phi < 2\pi\ \&\&\ |\eta| < 1.0)} \tag{3.27}$$

Effective ε_{rec} and ε_{acc}

$$\varepsilon_{rec}^{eff} = \frac{reconstructed\ \&\ extracted\ \pi^0}{\pi^0(1.40 < \phi_{\pi^0} < 3.15\ \&\&\ |\eta_{\pi^0}| < 0.65)} \tag{3.28}$$

$$\varepsilon_{acc}^{eff} = \frac{\pi^0(1.40 < \phi_{\pi^0} < 3.15\ \&\&\ |\eta_{\pi^0}| < 0.65)}{\pi^0(0 < \phi < 2\pi\ \&\&\ |\eta| < 1.0)} \tag{3.29}$$

where $1.40 < \phi < 3.15$ && $|\eta| < 0.65$ define a particle to be pointed at the EMCal. In the case of the pure efficiencies the decay products of the π^0 are required to fall into the EMCal acceptance whereas for the effective efficiencies the π^0 itself must be pointed at the EMCal. Additionally, the total correction to the data (to $\Delta\eta = 2$) is

$$\frac{1}{Total\ Correction} = \varepsilon_{rec}^{pure} \times \varepsilon_{acc}^{pure} = \varepsilon_{rec}^{eff} \times \varepsilon_{acc}^{eff}. \tag{3.30}$$

An extremely important point to note is that these quantities correct the data to two full units of rapidity. Therefore, in the determination of $\mathrm{d}N/\mathrm{d}y$ there is an additional factor of 0.5 applied to the data. The calculations are defined this way since the EMCal acceptance is larger than one unit of rapidity: $\Delta y = 1.30$ and it's conceptually unintuitive to have an efficiency which *could* be greater than 1.
In general, the reconstruction efficiency, ϵ_{rec}, is the product of all the efficiencies due to the detector setup and reconstruction algorithms. This includes

- Detector dead areas and noisy channels
- EMCal clustering algorithms
- Photon identification
- Inefficiencies of the yield extraction procedure.

To correct for these inefficiencies a full scale Monte Carlo simulation were run using the GEANT3 [41] framework developed at CERN, as discussed in Section 3.2.2. With the simulated knowledge of what a given input to the detector/reconstruction software should render as output, an overall efficiency for the effects listed above can be constructed.
The *pure* and *effective* corrections (previously defined) are shown in Figure 3.16 left and right respectively.

3.7 Secondary Pion Correction

To assist theorists in comparing π^0 predictions to the final spectra from data, a secondary pion correction (so called "feed down“) is applied to the final dataset.
To distinguish “feed down” $\pi^0 s$ from “primary” $\pi^0 s$ in Monte Carlo one can rely on the boundaries set by the generators in the decay chain, as all the generators used by ALICE are defined such that material interactions as well as decays from strange

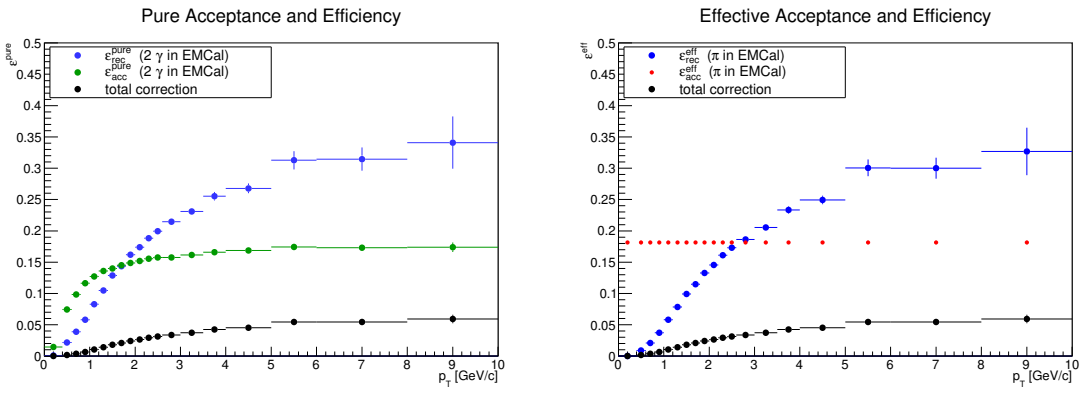

Figure 3.16: Pure reconstruction efficiency and acceptance correction (left) and effective reconstruction efficiency and acceptance correction. The flat acceptance efficiency is $\sim 18\%$ (right).

hadrons are handle by GEANT3 and not the original decayer for instance in Pythia or Phojet. This definition would correspond to a decay radius cut of approximately 1cm except for the strange hadrons where all decays are treated as secondaries.
For $\pi^0 s$ in this analysis, the following distinctions [43] are made:

Primary

Prompt particles produced in the collision including all decay products, except products from weak decays of light flavor hadrons (hadron whose valence quarks consist only of u, d, and s quarks) and of muons. These are identified by checking that the π^0 is on the produced by the generator and not GEANT3.

Secondary

Any π^0 *not* on the produced by the generator. These can be split into two categories:

Secondary from weak decay

A daughter particle from a weak decay of a light flavor hadron or of a muon. For convenience, within the context of this analysis, these are identified as any secondary π^0 *not* from material (see below). Additionally, this category is subdivided into those $\pi^0 s$ whose parent is a K^0_s and "others".

Secondary from material

All particles except primaries and secondaries from weak decays. These are $\pi^0 s$ that are created by some long-lived particle's interaction with the detector material (including air). For convenience, within the context of this analysis,

these are identified as any secondary π^0 whose parent is a p, n, $K^{\pm}$ or $\pi^{\pm}$. [2]

Physical

Particles coming from some "physics" related to the collision (as opposed to some process related to the material). They are identified either as the product of primaries and secondaries from weak decays *or* the different between inclusive $\pi^0 s$ and secondaries from decays.

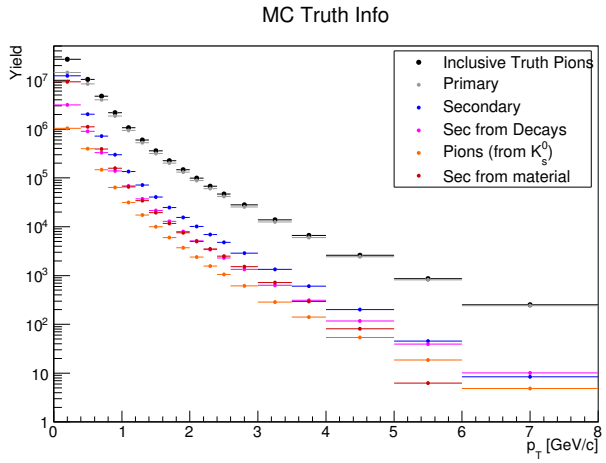

Figure 3.17: MC truth p_{T} spectra.

The relative amount of primary and secondary $\pi^0 s$ are taken from the Monte Carlo simulations used for the efficiency correction, LHC12f1a and LHC12f1b. However, it has been shown that the generation rate of K^0_s in both PYTHIA and PHOJET do not match the measured rates in data at both $\sqrt{s} = 900$ GeV [44] and $\sqrt{s} = 7$ TeV [45, 46]. Figure 3.18 shows the discrepancy for both energies. Above a K^0_s momentum of ~ 1 GeV/c, the relevant range affecting π^0 production, the K^0_s is underestimated by the MC by $\sim 40\%$ (a ratio of ~ 0.6) at $\sqrt{s} = 900$ GeV and underestimated by $\sim 25\%$ (a ratio of ~ 0.75) at $\sqrt{s} = 7$ TeV. A linear extrapolation performed in [47] estimates that the yield would be underestimated by $\sim 31\%$ (a ratio of ~ 0.69) at $\sqrt{s} = 2.76$ TeV. A systematic uncertainty (K^0_s discrepancy not known to within a factor of 2) is associated with this estimation (Section 3.8.7).

In addition, the overall pion yield in data and MC is not in perfect agreement. Figure 3.19 shows the raw reconstructed $\frac{\mathrm{d}N}{\mathrm{d}p_{\mathrm{T}}}$ for $\pi^0 s$ in both data and Monte Carlo

[2] This definition is not precisely correct since a $K^{\pm}$ can decay into a π^0. However, since the definition is held to be self-consistent within the analysis, the final difference is negligible. Ultimately, all $\pi^0 s$ which have a $K^{\pm}$ as their mother, whether via decay or material, are removed from the final sample.

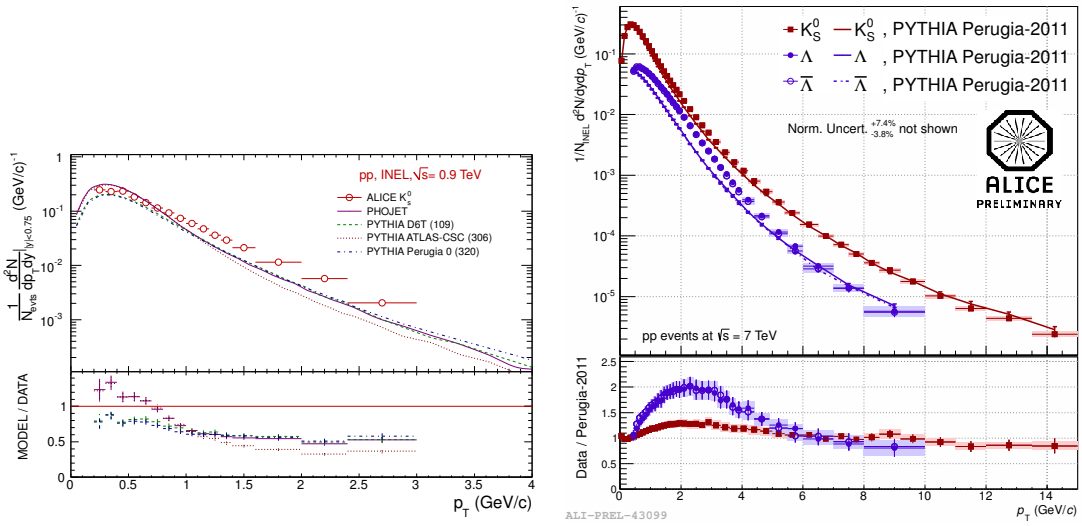

Figure 3.18: K^0_s discrepancy between data and MC at $\sqrt{s} = 900$ GeV (left panel) [44] and $\sqrt{s} = 7$ TeV (right panel) [45].

simulations. The ratio of Monte Carlo/data is shown in the lower panel along with a constant fit illustrating that the π^0 generation in the MC is underestimated by $\sim 20\%$ (a ratio of ~ 0.80).

Therefore, the Feed Down Fraction (FDF) must be constructed to correct for these

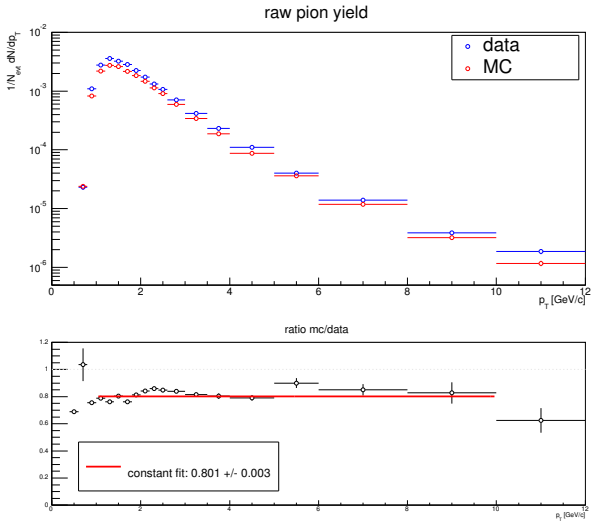

Figure 3.19: Raw π^0 discrepancy between data and MC.

discrepancies. The FDF is the relative amount of feed down $\pi^0 s$ in the fully corrected sample and defined as

$$FDF = \frac{C_{K^0_s} \cdot N^{\pi^0}_{K^0_s} + C_{\pi^0} \cdot N^{\pi^0}_{other\ decays}}{C_{\pi^0} \cdot N^{\pi^0}_{primary} + C_{K^0_s} \cdot N^{\pi^0}_{K^0_s} + C_{\pi^0} \cdot N^{\pi^0}_{other\ decays}} \tag{3.31}$$

$$= \frac{\frac{C_{K^0_s}}{C_{\pi^0}} \cdot N^{\pi^0}_{K^0_s} + N^{\pi^0}_{other\ decays}}{N^{\pi^0}_{primary} + \frac{C_{K^0_s}}{C_{\pi^0}} \cdot N^{\pi^0}_{K^0_s} + N^{\pi^0}_{other\ decays}} \tag{3.32}$$

where

$$C_{K^0_s} = \frac{N^{data}_{K^0_s}}{N^{MC}_{K^0_s}} = 1.45 \qquad \text{and} \qquad C_{\pi^0} = \frac{N^{data}_{\pi^0}}{N^{MC}_{\pi^0}} = 1.25 \qquad \text{so that} \qquad \frac{C_{K^0_s}}{C_{\pi^0}} = 1.16 \tag{3.33}$$

The FDF is subtracted from the cross section (Equation 3.35):

$$E\frac{\mathrm{d}^3\sigma}{\mathrm{d}p^3} = \frac{1}{2\pi}\frac{1}{p_\mathrm{T}}\frac{\sigma_{MB}}{N_{evt}}\frac{1}{A \cdot \varepsilon_{rec}}\frac{1}{BR_{\pi^0\to\gamma\gamma}}\frac{\mathrm{d}N^{\pi^0}}{\mathrm{d}p_\mathrm{T}\mathrm{d}y}(1 - FDF) \tag{3.34}$$

This formulation is valid as long as the efficiency to reconstruct the various types of physical $\pi^0 s$ is the same. Figure 3.20 shows the effective reconstruction efficiency for various identified sources (primary, physical, all decay secondary, and secondary only from K^0_s decays). All types have the same reconstruction efficiency. This is not surprising since the majority of decay pions happen within $\sim$ 50 cm of the collision. Figure 3.21 shows the production radius for various categories of $\pi^0 s$. Most $\pi^0 s$ originating beyond a radius of $\sim$ 50 cm are material $\pi^0 s$ and are therefore removed by the reconstruction efficiency correction. Moreover, since the resolution

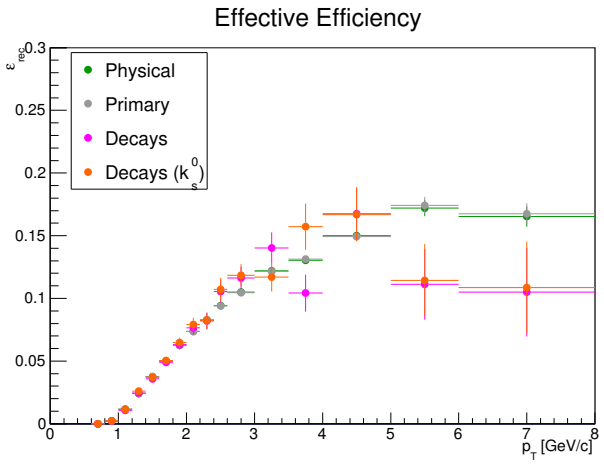

Figure 3.20: Raw π^0 discrepancy between data and MC.

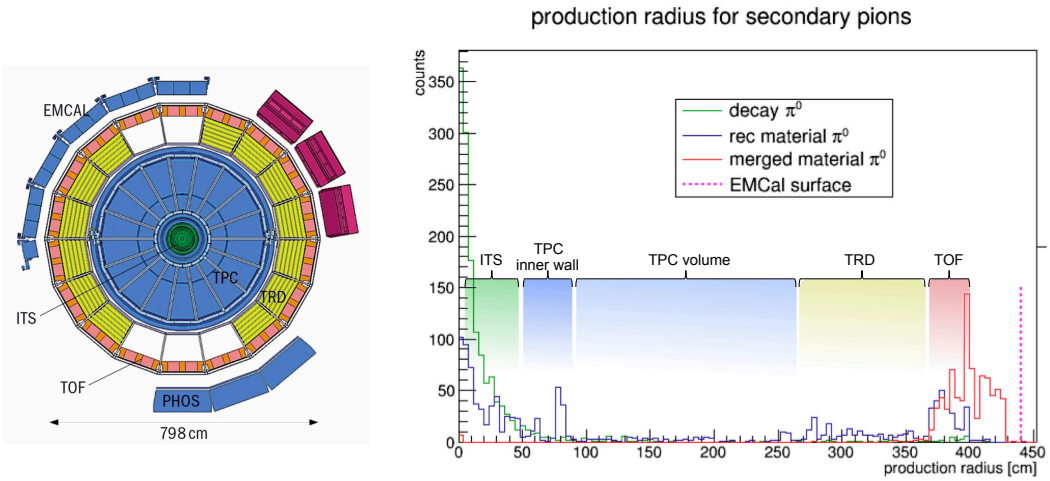

Figure 3.21: Production radii for various categories of $\pi^0 s$.

of the EMCal dictates that the mass resolution of the π^0 is between 8 and 20% (typically $\sim$ 10%), most of the decay $\pi^0 s$ fall inside 3σ of the peak center. The typical integration window for counting $\pi^0 s$ is $2.5 - 3\sigma$. Figure 3.22 shows the correlation between production radius and reconstructed mass for secondary $\pi^0 s$. A 3σ counting window would typically count all $\pi^0 s$ between roughly 90 and 180 MeV/c^2, thus illustrating why the efficiencies for all physical $\pi^0 s$ are the same. The final FDF that is applied to the data is shown in Figure 3.23. The brown

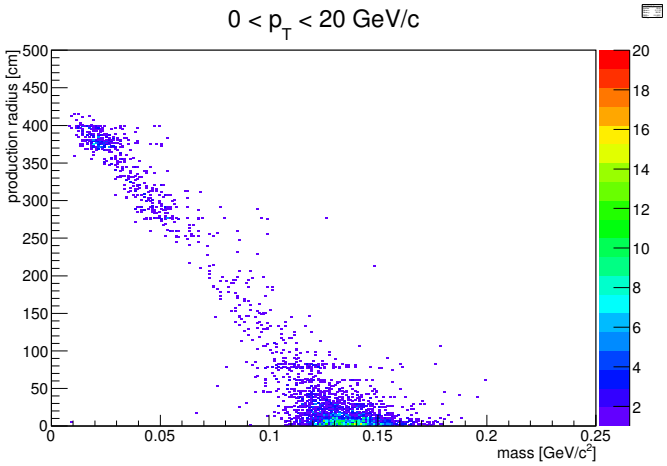

Figure 3.22: Secondary π^0 production radius vs reconstructed mass.

points are the K_s^0 contribution of the FDF, before (open) and after (closed) the K_s^0 modification. The blue points are the total FDF, before (open) and after (closed) the K_s^0 is fixed. The closed blue points are fit to an arbitrary function (convolution of two exponentials) for smoothing purposes. The red fit is what is finally applied

to the data.

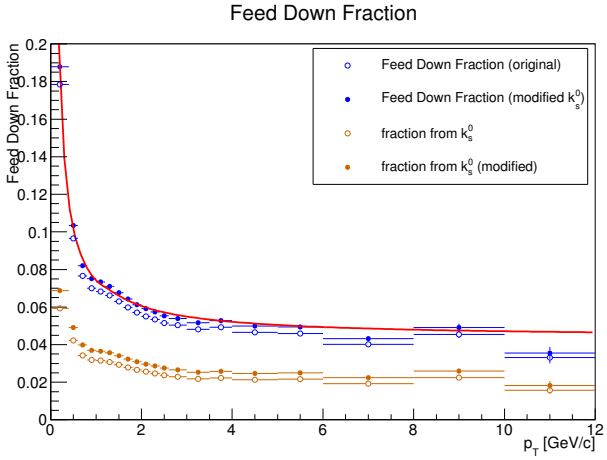

Figure 3.23: Fraction of neutral pions from feed down from different sources. The brown symbols show the fraction of neutral pions from K^0_s as obtained from the Monte Carlo simulation (open circle) and after modification according to the data (closed circle). The blue symbols show the total correction needed with the red line as a fit to the closed blue points

3.7.1 Bin Width Corrections

The final spectrum must be corrected for the bin widths. The data is normalized to $\frac{dN}{dp_T dy}$. Therefore, we divide by the p_T bin width and the rapidity gap, $\Delta y = 2$ (see Section 3.6.1). Since the data is corrected up to the full azimuth, we additionally divide by 2π (equivalent to the bin width in φ).

3.8 Systematic Uncertainty

There are various stages where some systematic uncertainty can creep into the measurement. Quantitatively reporting all these sources can be tricky since we are attempting to quantify something that we inherently *do not* know. The typical (though not only) strategy is to vary some parameter (cuts, thresholds, etc) within some reasonable degree such that we expect to get the same (and hopefully correct!) answer and then observe the systematic variation of the answer. The following sources of systematic uncertainty are considered:

- Clusterizer: compare 4 different clusterization schemes.
- Cluster cuts, bkg subtraction: compare different cuts and bkg subtraction techniques.
- Yield extraction: compare 3 different fit functions with "simple" counting.
- Non-linearity correction: vary non-linearity scheme.
- Energy scale: compare mass position in data and MC.
- Efficiency correction: compare PYTHIA8 and PHOJET MC generators.
- Material budget: Loss of neutral pions due to conversions in the TRD and TOF and gain of pions due to creation in the material of these detectors.
- Feed-down correction: vary k_s^0 contribution.

An approximate summary of the magnitudes of the various contributions is shown in Table 3.24 while the various components are plotted in Figure 3.25. Each contribution will be explained in the following sections.

Systematic Uncertainty Component	Relative Uncertainty $p_{\mathrm{T}} \lesssim 1.5$ (GeV/c)	Relative Uncertainty $p_{\mathrm{T}} \gtrsim 1.5$ (GeV/c)
clusterizer	2−10%	2−4%
cluster cuts, bkg sub	6%	6%
yield extraction	2−8%	1.5%
non-linearity correction	3.5%	3.5%
energy scale	3%	3%
efficiency correction	3−10%	3−4%
acceptance	5%	5%
material budget	1−2%	$< 2\%$
feed-down correction	2%	2%
total uncertainty	15%	12%

Figure 3.24: Table of systematic uncertainties for two transverse momentum bins.

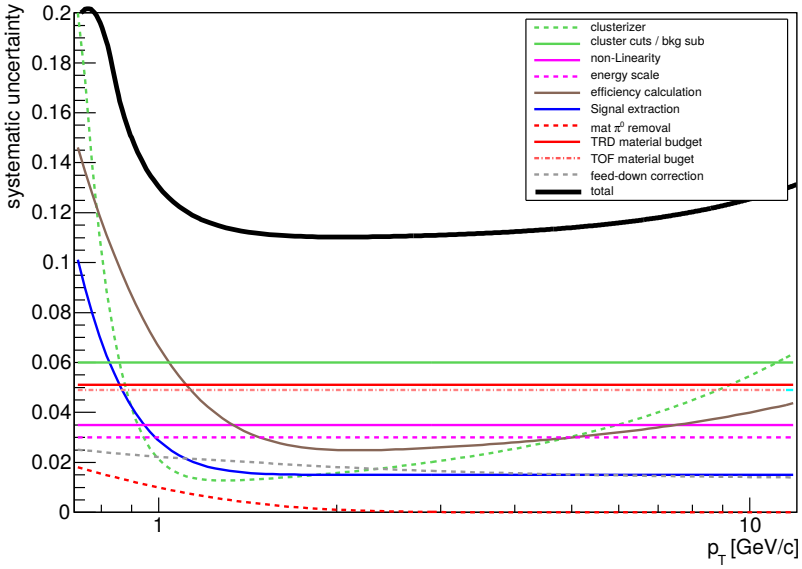

Figure 3.25: Summary of Systematic Uncertainty.

3.8.1 Clusterization

In order to get access to the systematic error clusterizer the identical analysis has been performed using 4 different clusterization schemes:

- With a seed threshold of 100 MeV using the V1 clusterizer called “100v1”.
- With a seed threshold of 100 MeV using the V2 clusterizer called “100v2”.
- With a seed threshold of 300 MeV using the V1 clusterizer called “300v1”.
- With a seed threshold of 300 MeV using the V2 clusterizer called “300v2”.

For each of those variations a minimum cell energy threshold of 50 MeV is required. After having done the full analysis including all corrections the cross-sections are compared as shown in Figure 3.26 with a ratio to a combined fit shown in the lower panel.

The maximum spread of the clusterizers at each p_{T} is plotted in the right panel

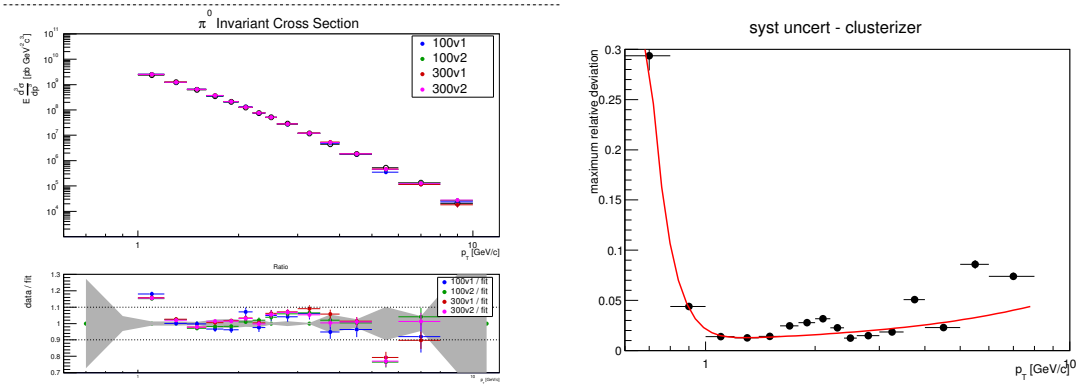

Figure 3.26: Comparison of various clusterization schemes to ascertain the systematic uncertainty due to the choice of the clusterizer and its settings (left). Maximum relative deviation to the fit of the average of the different clusterizations schemes (right).

of Figure 3.26. To smooth the distribution, an arbitrary function (exponential + polynome of order 1) is fitted to the points. The large statistical uncertainty at high p_{T} is ignored. The red curve in Figure 3.26 is used as the systematic uncertainty due to the clusterizer choice. It should be noted that this is a conservative estimate since the maximum deviation of the points are used. In principle, the RMS could be taken instead.

3.8.2 Cluster Cuts & Background Subtraction

To estimate the error due to the mismatch of the cluster description in the data and the Monte Carlo, all cuts imposed on the clusters have been varied. These cuts are:

- the minimum number of cells per cluster
- the minimum energy of the clusters
- the elongation of the cluster represented by λ_0^2 and λ_1^2
- the minimum distance to bad or noisy channels in the calorimeter
- the track matching to the fully reconstructed charged tracks in the central barrel of ALICE

Additionally different schemes for the rejection of the background have been explored, like the common scaling of the mixed event background with a polynomial and the polynomial fitting of the sidebands next to the peak. Reasonable variations on those parameters lead to an upper estimate of the cluster description systematic error of 6%, being the largest systematic error source above $p_{\mathrm{T}} = 1.2$ GeV/c.

3.8.3 Yield Extraction

The systematic uncertainty on the yield extraction is assessed by performing the full analysis using 4 different methods to 'count' the number of detected pions. The first (and default) is a simple counting approach where the background-subtracted signal histogram is integrated between $\pm 3.5\sigma$ of a gaussian fit to the peak. The residual background (estimated by a simple pol1) is additionally subtracted. This 'counting method' is used as the baseline to compare 3 other methods. The peak is fit using gaussian, asymmetric gaussian, and crystal ball functions (see Section 3.4). The results are shown on the left panels in Figure 3.27, where the lower panel is the ratio of each of the fit function methods to the counting method. The maximum spread of the points at each p_{T} is plotted in the right panel of Figure 3.27. To smooth the p_{T} dependence of the uncertainty, an arbitrary function (exponential + constant) is fitted and shown as the red curve; this red curve is used as the systematic uncertainty. As for the variation of the clusterizer the conservative approach of using the maximum deviation was used.

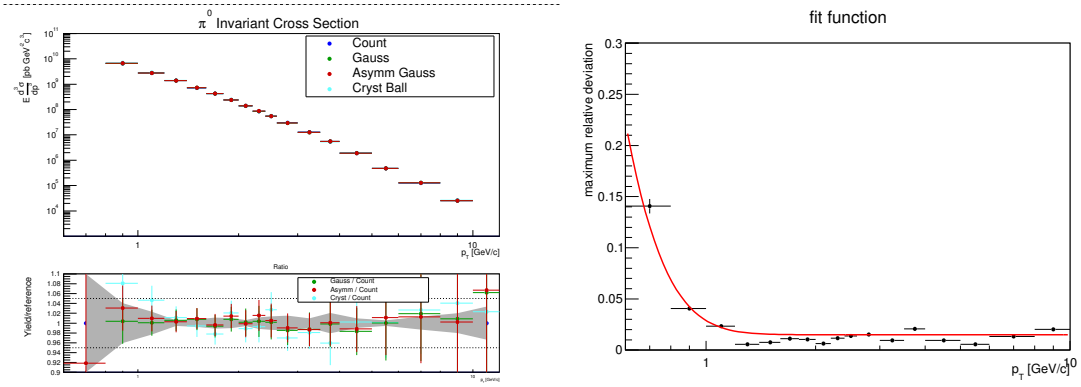

Figure 3.27: Comparison of various yield extraction method to estimate the systematic error due to the choice of the extraction technique with the lower panel being the ratio to the standard ("Counting") approach (left). The maximum deviation for each transverse momentum bin derived from this variations is show on the right together with the final systematic error arising from these variations.

3.8.4 Non-linearity Correction & Energy scale

As already described Section 3.3.1 the systematic error on the choice of the non-linearity correction can be calculated by rerunning the analysis with the different non-linearity correction discussed there. From those variations a systematic error of 3.5% was estimated.

For the energy scale uncertainty on the other had the π^0 and η peak positions in data and Monte Carlo simulation can be compared. The ratio of the two mass positions, which were each obtained using a Gaussian fit can be seen in Figure 3.28. There is very good agreement for both mesons, with the discrepancy being less than 0.5%. Since a 1% shift in the π^0 p_{T} corresponds to a $4-5$% change in the yield, a conservative flat 3% systematic uncertainty is assigned to the energy scale.

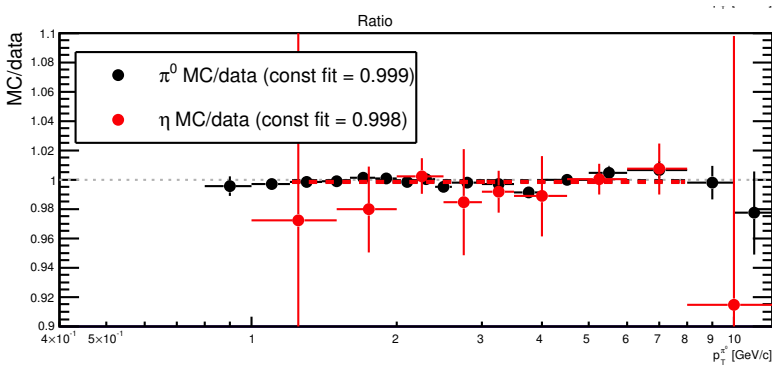

Figure 3.28: MC/data peak position ratio for Systematic Uncertainty.

3.8.5 Reconstruction Efficiency Correction

To determine the consistency between the Monte Carlo simulations to calculate the reconstruction efficiency, the full analysis was run (for 3 different clusterizer schemes) using the two available Monte Carlo datasets separately. As a reminder, LHC12f1a uses PYTHIA8 for the generator while LHC12f1b uses PHOJET . The ratio of LHC12f1a/LHC12f1b is shown in the left panel of Figure 3.29. The right panel shows the absolute value of the difference from unity overlaid with an arbitrary smoothing function (exponential + pol1).

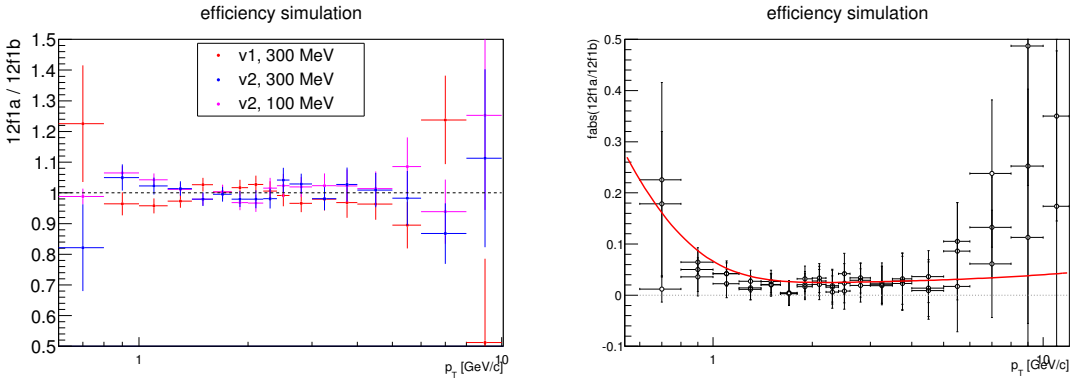

Figure 3.29: The ratio of LHC12f1a/LHC12f1b is plotted in the left panel for 3 different clusterization schemes; the right panel shows the absolute value of the deviation from unity as well as a smoothing function (exponential +pol1).

3.8.6 Material Budget

The final π^0 yield is affected in two ways by the material. First, there is an increase due to additional $\pi^0 s$ being created through interactions of high-energy particles with the material. Secondly, there is a decrease in the yield due to an efficiency loss from photon conversions in the detector material. Conversions at smaller radii (*ie.* inside the outer wall of the TPC are very well modeled by the Monte Carlo [47] and thus does not need to be taking into account here). Conversions at larger radii on the other hand are more likely to merge as they get closer to the EMCal surface and thus their reconstruction efficiency will be higher compared to the ones at low radii. This process however depends strongly on the position of the material in which those photons convert and thus needs to be modeled correctly in the GEANT3 simulations.

The first effect can be addressed following the work in [48], the material budget

outside the TPC is known to better than 10%. Applying this 10% uncertainty to the fraction of $\pi^0 s$ that are created in the material (left panel of Figure 3.30, the uncertainty due to the presence of the TRD and TOF is less than 2% above 1 GeV/c (right panel of Figure 3.30. For the remaining uncertainty the acceptance of the EMCal has been split into two regions:

a) where we have TRD modules in front of the detector

a) where we have no TRD modules yet in front of the detector

In the data taking period of considered in this thesis not all TRD modules have been installed yet and only 2/5 of the EMCal actually had it in front of them, thus allowing us to fully reconstruct the neutral pions in those two region. Afterwards the resulting fully corrected spectra have been compared and a systematic offset of 5% has been found. According to [49, 50] approximately the same amount of material, however these blocks of material are much closer to the EMCal and thus conversion will most likely merge into one cluster. Under the assumption that both detectors are modeled with approximately the same accuracy an additional error of 3% for the material budget in the TOF has been assigned.

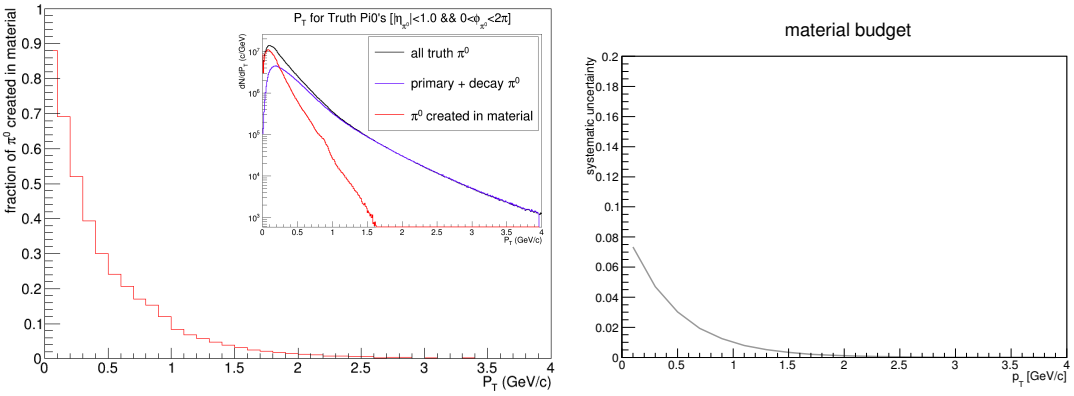

Figure 3.30: Systematic uncertainty on the production of additional neutral pions in the TRD and TOF via interactions with the detector material.

3.8.7 Feed Down Correction

The feed down correction is discussed in great detail in Section 3.7. The assumption for the systematic uncertainty is that the correction to the FDF for the K_s^0 discrepancy between data and Monte Carlo could be wrong by a factor of 2 (probably a gross overestimation). The K_s^0s make up roughly half of the feed down contributions. Moreover, the K_s^0 component in the FDF is corrected up by 16%. Therefore,

assuming that this correction could be wrong by a factor of 2, this would lead to an uncertainty on the FDF of $\sim 8\%$. We conservatively round this up to 20%. It should be noted that this results in an approximately-flat contribution to the overall systematic uncertainty of only $\sim 2\%$, negligible compared to nearly any other component, thus not appreciably affecting the final result. Figure 3.31 shows the result of a 20% uncertainty applied to the FDF.

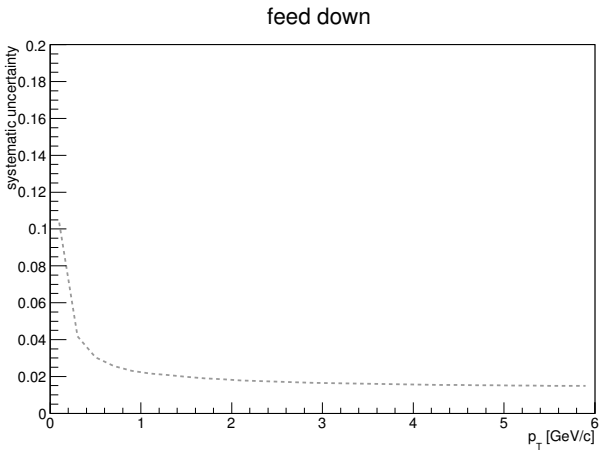

Figure 3.31: Systematic uncertainty arising from the secondary pion correction.

3.9 Results

The differential invariant cross section for neutral pions can be calculated according to

$$E\frac{\mathrm{d}^3\sigma}{\mathrm{d}p^3} = \frac{1}{2\pi}\frac{1}{p_{\mathrm{T}}}\frac{\sigma_{MB}}{N_{evt}}\frac{1}{A\cdot\varepsilon_{rec}}\frac{1}{BR_{\pi^0\to\gamma\gamma}}\frac{\mathrm{d}N^{\pi^0}}{\mathrm{d}p_{\mathrm{T}}\mathrm{d}y} \tag{3.35}$$

from the various inputs previously discussed.

This fully corrected invariant cross section can then be compared to measurements in other detection channels [1] and a new combined average can be calculated according to the BLUE-method. The comparison of the individual measurement to a fit to the combined spectrum is shown in Figure 3.32. All three independent measurement agree within ±10% with the combined measurement. Additionally the

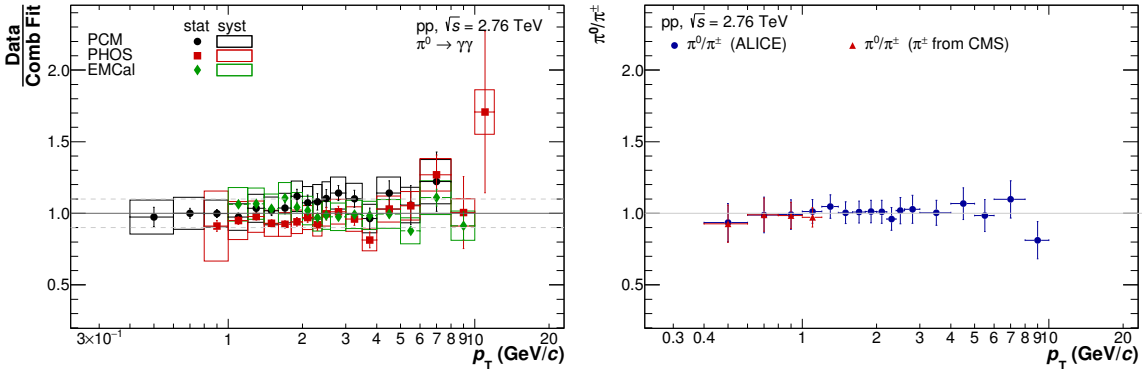

Figure 3.32: Ratio of three independent π^0 meson measurements in pp collisions at $\sqrt{s} = 2.76$ TeV to the fit of the combined normalized invariant production cross section at this energy (left) and of the combined measurement to the charged pion results (right). For the later the errors are the quadratic sum of the statistical and systematic errors of both measurements.

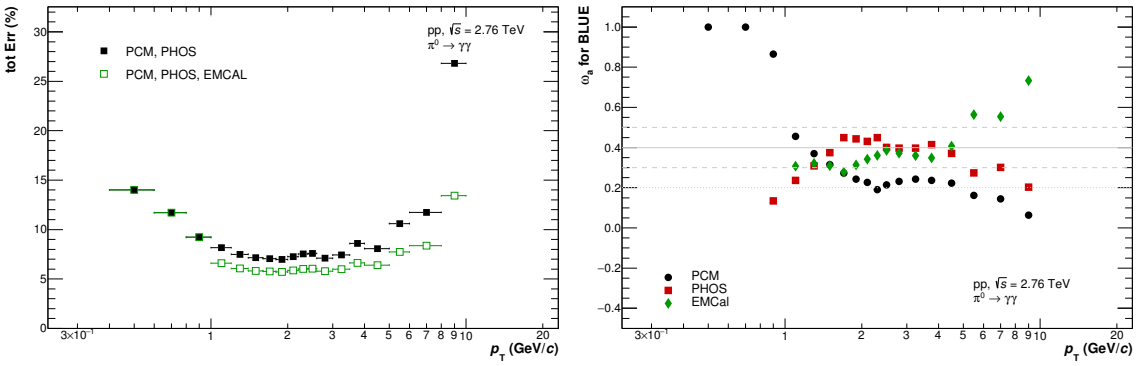

Figure 3.33: Comparison of the total systematic and statistical errors summed in quadrature for the combination of the neutral pion measurement via PCM and PHOS, or all three available measurements.

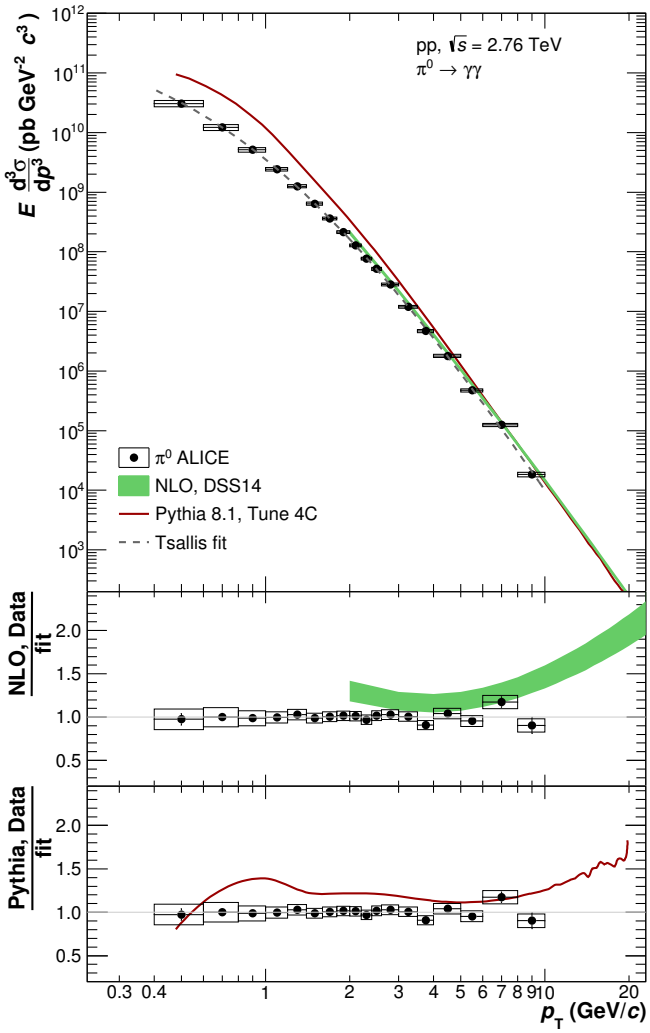

Figure 3.34: Comparison of the combined measured invariant cross section of neutral pions with Pythia 8 calculations, run with the Tune 4C, and M. Strattmanns pQCD NLO caluclations.

combined measurement can be compared to the charged pion results [3] and it is found to be in good agreement with this measurement as well.

This new measurement via the EMCal of the neutral pion improves the total error of the measured transverse moChargedPionsmentum invariant cross section by a factor of 1.3, as seen in Figure 3.33 (left). At high transverse momentum the measurement in the EMCal completely takes over due its significantly reduced statistical errors. The right plot of Figure 3.33 shows the respective weights of the individual measurements versus transverse momentum. It is clearly seen that the strength of the measurement by the EMCal is comparable in the momentum region from 1 GeV/c $< p_{\mathrm{T}} <$ 4 GeV/c and then it starts taking over. The final spectrum is then compared to Pythia 8 calculations with the Tun 4C and the calculations by M. Strattmann [2] in Figure 3.34

CHAPTER 4

Summary and outlook

The main work presented in this thesis is the measurements of the neutral pion yield and its invariant cross section as a function of transverse momentum in pp collisions at a center-of-mass energy of $\sqrt{s}$= 2.76 TeV with ALICE EMCal detector.
The $\pi^0 s$ are measured in the two photon decay channel and photons are reconstructed via the energy deposit in the EMCal. To obtain the π^0 yield, it is needed to extract the signal from the invariant mass distribution of photon pairs by subtracting the combinatorial background which is calculated mainly via the mixed events technique. The measurement of π^0 spectra can reach to 10 GeV limited by the statistic and energy deposit overlap in the EMCal.
Additionally, the production yield of neutral pions can be measured in the same detection channel by using the PHOS and the photon conversion method to reconstruct the photons. This allows to compare the neutral pion measurements presented in this thesis to the measurements by PHOS and PCM. As they all agree within $\pm$10% they can be combined using the BLUE method, which reduces the errors of the combined measurement with respect to the single measurements by a factor of ≈ 2. The combined measurement can then be compared to the charged pion results and it is found to be in good agreement with this measurement as well.
This measurements of neutral pion spectra in pp collisions at $\sqrt{s}$ = 2.76 TeV presents important data for perturbative QCD (pQCD) calculations and gluon frag-

mentation functions. Furthermore it provides a reference to study the properties of the hot and dense medium (QGP). In particular it is needed for the calculation of parton energy loss via the nuclear modification factor.

To further understand the underlying physics the measurement can be extended to higher transverse momenta by using the cluster-splitting method. In addition to that both neutral pion reconstruction methods can be applied to the data collected in p–Pb and Pb–Pb collisions at the LHC, as well as to pp collisions at different center-of-mass energies.

The π^0 decay kinematics shows that the opening angle of the two decay photons from neutral pion gets smaller with increasing neutral pion energy due to the Lorentz boost. For the case of EMCal in ALICE, the two electromagnetic showers coming from the two decay photon begin to overlap if the energy of π^0 is greater than 5-6 GeV or 10 GeV, for the two main clusterizers, respectively. A new method can be used to identify π^0, which is based on the differences of shape between the overlapping photon shower and single photon shower. One can expect that the measurements of π^0 can be extended to very high transverse momenta of about 40 GeV by using this method.

CHAPTER 5

Acronyms and Technical Terms

ALICE	A Large Ion Collider Experiment
AOD	Analysis Object Data
APD	Avalanche Photo Diode
BLUE	Best Linear Unbiased Estimate
CERN	European Organization for Nuclear Research
DPM	Dual Parton Model
EMCal	Electromagnetic Calorimeter
ESD	Event Summary Data
FEE	Front End Electronics
FDF	Feed Down Fraction
FPGA	Field Programmable Gate Array
GEANT	Geometry and Tracking Software
ITS	Inner Tracking System

L1	level-1
LHA	Les Houches Accord
LHC	Large Hadron Collider
LHEF	Les Houches Event Files
LQCD	Lattice QCD
NLO	Next-to-Leading Order
NNLO	Next-to-Next-to Leading Order
PDF	Parton distribution function
PHOS	Photon Spectrometer
PCM	Photon Conversion Method
PDF	parton density functions
pQCD	perturbative QCD
QCD	Quantum Chromodynamics
QED	Quantum Electrodynamics
QGP	Quark-Gluon Plasma
RHIC	Relativistic Heavy Ion Collider
RMS	root mean squared
SDD	Silicon Drift Detector
SDM	Symmetric Decay Method
SM	Standard Model
SPD	Silicon Pixel Detector
SPS	Super Proton Synchrotron
SSD	Silicon Strip Detector
STU	Summary Trigger Unit

TOF	Time-Of-Flight detector
TPC	Time Projection Chamber
TRD	Transition Radiation Detector
TRU	Trigger Region Unit
VZERO	V0 detector

CHAPTER 6

Appendix

6.1 Background Subtraction Plots

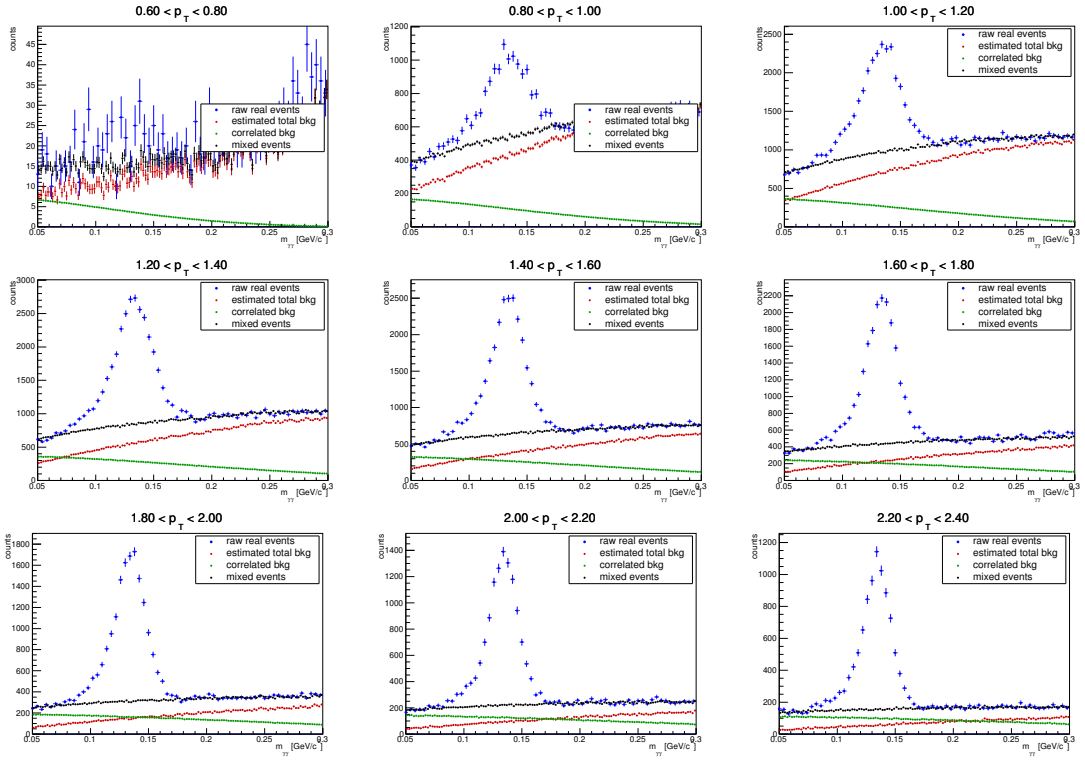

6.1. Background Subtraction Plots

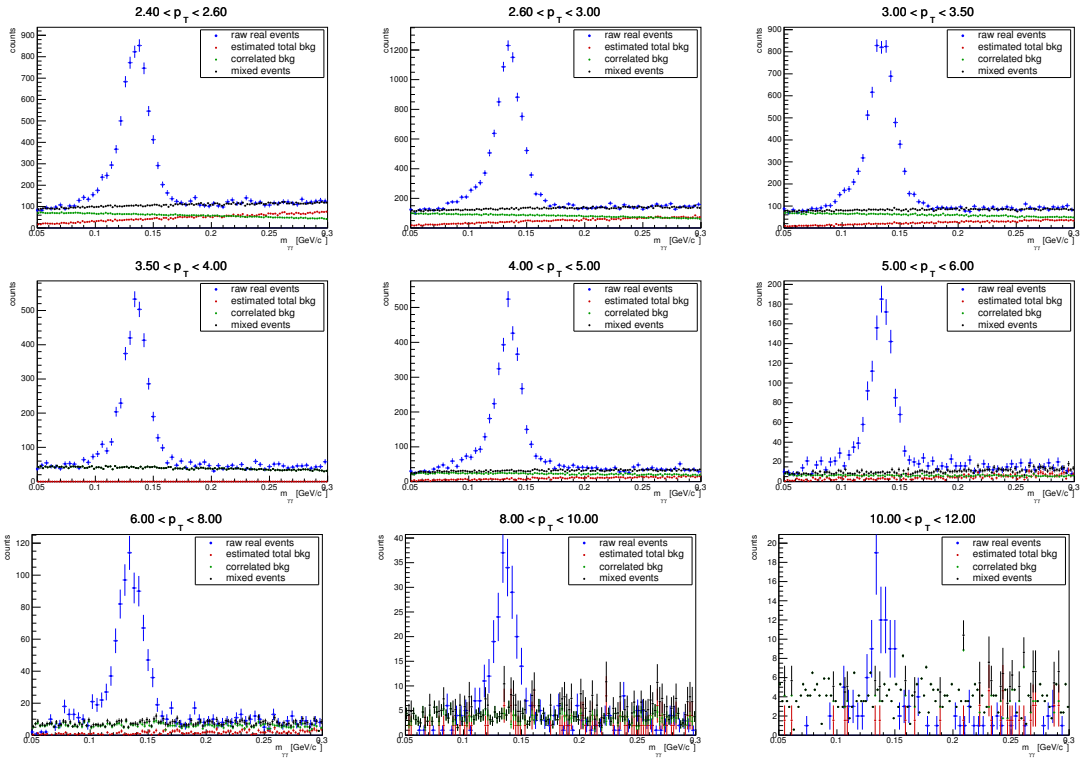

6.2 Raw Peak Extraction Plots

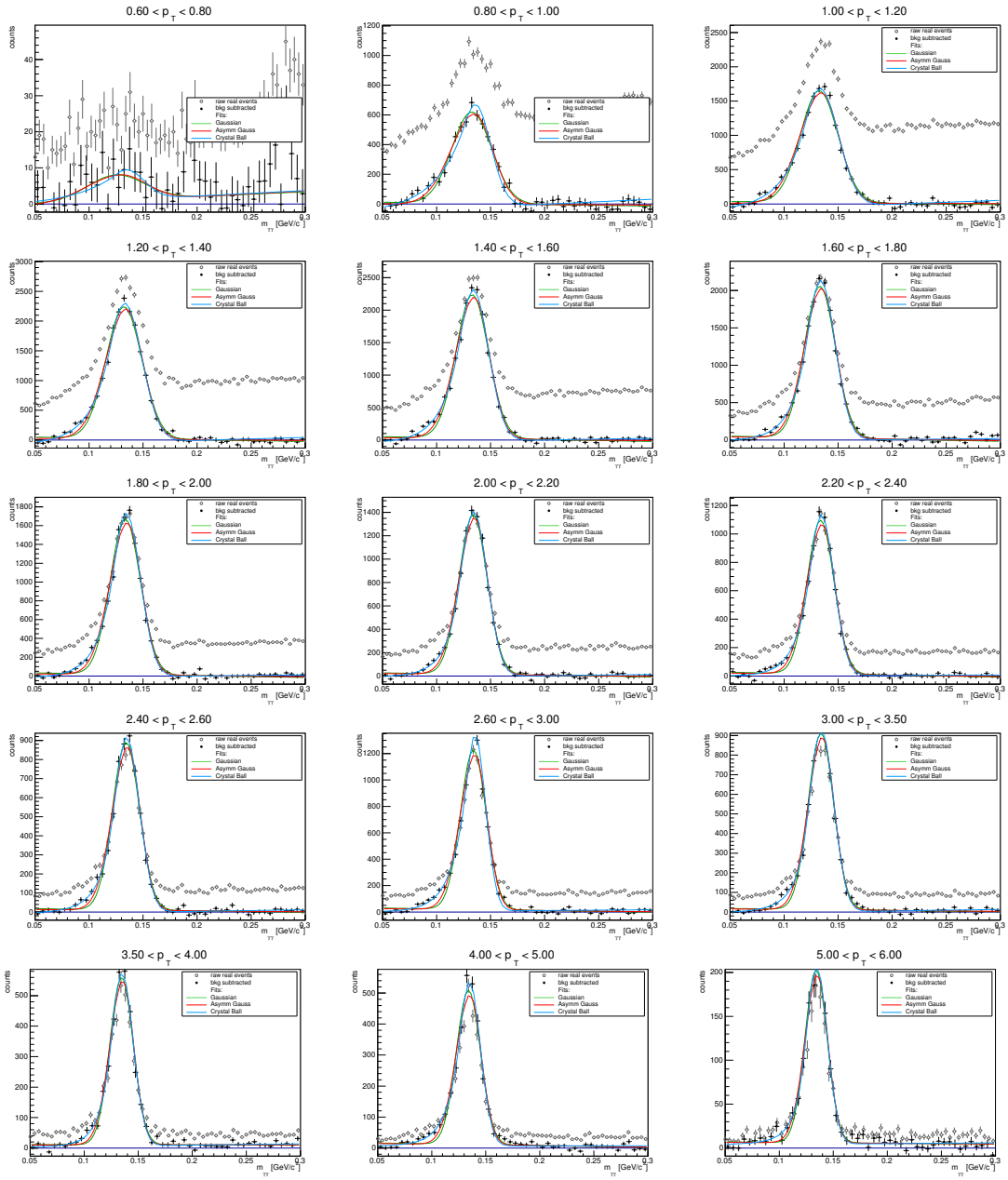

6.2. Raw Peak Extraction Plots

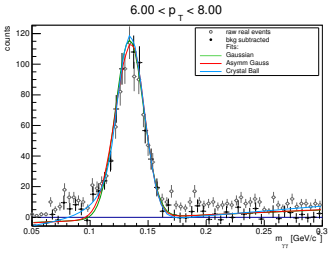

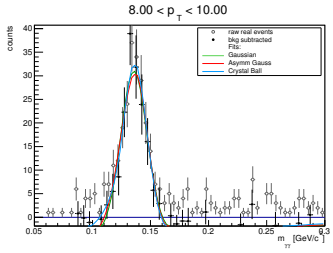

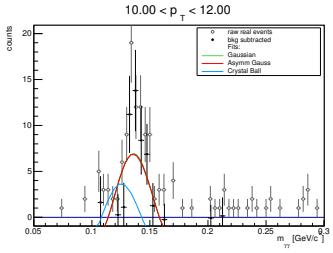

6.3 Neutral pion analysis framework

The analysis is the operation performed on the data and the users can extract interesting physics information. In the ALICE experiment, the analysis is proceeded based on AliRoot software framework. It starts from the Event Summary Data (ESD) produced during the reconstruction step. The Analysis Object Data (AOD) is produced with a very general analysis filter named *AliAnalysisTaskESDfilter* from the ESD (more filters can be done according to the user own for specific physics analysis from ESD or AOD). Further analysis passes can start from condensed AODs. The analysis chain in AliRoot can be found in Figure 6.1.

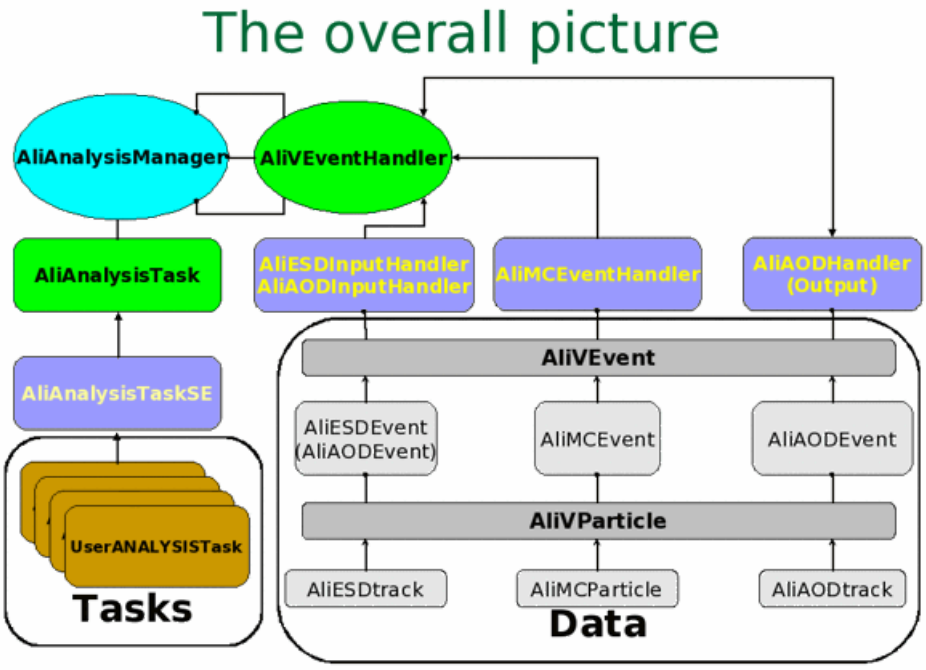

Figure 6.1: Schematic view of analysis framework starting from ESD and AOD data in AliRoot [51].

The neutral pion analysis in this work are analyzed with tasks located in two subdirectories in AliRoot:

- PWG/CaloTrackCorrBase
- PWGGA/CaloTrackCorrelations

In PWGGGA/CaloTrackCorrelations/macros, the analysis macros to launch the analysis can be found. The framework is rather flexible and allows to analyze particles, γ, π^0, η .

The analysis includes the following steps:

- **Event, cluster and track filtering**: Events are selected depending on the vertexes, centralities and other criteria tracks and calorimeter clusters are filtered based on the cuts required by the analyzer. The filtering is done in the class *AliCaloTrackReader*.

- **Neutral pion reconstruction**: Looping over the clusters, this selects the particles needed in the analysis with the corresponding PID criteria to the clusters. The particle with PID is put into a new array which will be the list of possible ations, or the invariant mass analysis for neutral mesons analysis. In our analysis, the triggers including γ, π^0 and η are identified via two different classes as:

  - γ **with** *AliAnaPhoton*: This class loops over all clusters in an array with the photon identification criteria, such as track matching, cluster timing, cluster shower shape cuts, etc to select the photon candidates for correlation or neutral mesons analysis.
  - π^0 (η) **with** *AliAnaPi0*: This class can perform invarant mass analysis of photon for neutral meson reconstruction.

Bibliography

[1] **ALICE Collaboration**, B. B. Abelev *et al.*, "Neutral pion production at midrapidity in pp and Pb-Pb collisions at $\sqrt{s_{\rm NN}} = 2.76\,\text{TeV}$", *Eur.Phys.J.* **C74** (2014), no. 10, 3108, arXiv:1405.3794.

[2] D. de Florian, R. Sassot, M. Epele, R. J. Hernandez-Pinto, and M. Stratmann, "Parton-to-Pion Fragmentation Reloaded", *Phys.Rev.* **D91** (2015), no. 1, 014035, arXiv:1410.6027.

[3] **ALICE Collaboration**, B. B. Abelev *et al.*, "Production of charged pions, kaons and protons at large transverse momenta in pp and Pb–Pb collisions at $\sqrt{s_{\rm NN}}$ =2.76 TeV", *Phys.Lett.* **B736** (2014) 196–207, arXiv:1401.1250.

[4] **Particle Data Group**, K. Olive *et al.*, "Review of Particle Physics", *Chin.Phys.* **C38** (2014) 090001.

[5] P. Skands, "Introduction to QCD", arXiv:1207.2389.

[6] G. 't Hooft, "A Planar Diagram Theory for Strong Interactions", *Nucl.Phys.* **B72** (1974) 461.

[7] D. J. Gross and F. Wilczek, "Ultraviolet Behavior of Nonabelian Gauge Theories", *Phys.Rev.Lett.* **30** (1973) 1343–1346.

[8] H. D. Politzer, "Reliable Perturbative Results for Strong Interactions?", *Phys.Rev.Lett.* **30** (1973) 1346–1349.

[9] E. V. Shuryak, "Quantum Chromodynamics and the Theory of Superdense Matter", *Phys.Rept.* **61** (1980) 71–158.

[10] K. G. Wilson, "Confinement of Quarks", *Phys.Rev.* **D10** (1974) 2445–2459.

[11] F. Karsch, "Lattice QCD at high temperature and density", *Lect.Notes Phys.* **583** (2002) 209–249, arXiv:hep-lat/0106019.

[12] F. Karsch, E. Laermann, and A. Peikert, "The Pressure in two flavor, (2+1)-flavor and three flavor QCD", *Phys.Lett.* **B478** (2000) 447–455, arXiv:hep-lat/0002003.

[13] J. M. Lattimer and M. Prakash, "Neutron Star Observations: Prognosis for Equation of State Constraints", *Phys.Rept.* **442** (2007) 109–165, arXiv:astro-ph/0612440.

[14] M. G. Alford, A. Schmitt, K. Rajagopal, and T. Schäfer, "Color superconductivity in dense quark matter", *Rev.Mod.Phys.* **80** (2008) 1455–1515, arXiv:0709.4635.

[15] M. A. Stephanov, "QCD phase diagram and the critical point", *Prog.Theor.Phys.Suppl.* **153** (2004) 139–156, arXiv:hep-ph/0402115.

[16] Y. Aoki, G. Endrodi, Z. Fodor, S. Katz, and K. Szabo, "The Order of the quantum chromodynamics transition predicted by the standard model of particle physics", *Nature* **443** (2006) 675–678, arXiv:hep-lat/0611014.

[17] e. Evans, L. and e. Bryant, P., "LHC Machine", *JINST* **3** (2008) S08001.

[18] **ALICE Collaboration**, K. Aamodt *et al.*, "The ALICE experiment at the CERN LHC", *JINST* **3** (2008) S08002.

[19] B. Alessandro, F. Antinori, J. Belikov, C. Blume, A. Dainese, P. Foka, P. Giubellino, B. Hippolyte, C. Kuhn, G. Martínez, *et al.*, "ALICE: Physics performance report, volume II", *Journal of Physics G: Nuclear and Particle Physics* **32** (2006) 1295–2040.

[20] P. Kuijer, "Commissioning and Prospects for Early Physics with ALICE", *Nucl.Phys.* **A830** (2009) 81C–88C, arXiv:0907.5060.

[21] **ALICE Collaboration**, G. Dellacasa *et al.*, "ALICE technical design report of the inner tracking system (ITS)", 1999.

[22] **ALICE Collaboration**, B. Abelev *et al.*, "Measurement of charm production at central rapidity in proton-proton collisions at $\sqrt{s} = 7$ TeV", *JHEP* **1201** (2012) 128, arXiv:1111.1553.

[23] **ALICE Collaboration**, B. Abelev *et al.*, "Suppression of high transverse momentum D mesons in central Pb-Pb collisions at $\sqrt{s_{NN}} = 2.76$ TeV", *JHEP* **1209** (2012) 112, arXiv:1203.2160.

[24] **ALICE Collaboration**, G. Dellacasa *et al.*, "ALICE: Technical design report of the time projection chamber", 2000.

[25] **ALICE Collaboration**, G. Dellacasa *et al.*, "ALICE technical design report of the photon spectrometer (PHOS)", 1999.

[26] M. Ippolitov, S. Beloglovsky, M. Bogolyubsky, S. Burachas, S. Erin, *et al.*, "Studies of lead tungstate crystals for the ALICE electromagnetic calorimeter PHOS", *Nucl.Instrum.Meth.* **A486** (2002) 121–125.

[27] **ALICE PHOS calorimeter**, D. Aleksandrov *et al.*, "A high resolution electromagnetic calorimeter based on lead-tungstate crystals", *Nucl.Instrum.Meth.* **A550** (2005) 169–184.

[28] **ALICE Collaboration**, P. Cortese *et al.*, "ALICE electromagnetic calorimeter technical design report", 2008.

[29] **ALICE Collaboration**, P. Cortese *et al.*, "ALICE technical design report on forward detectors: FMD, T0 and V0", 2004.

[30] "Beam parameters". http://lpc.web.cern.ch/lpc/fillingschemes.htm

[31] R. Engel, "Phojet manual", *University of Siegen preprint*, 1995 95–05.

[32] R. Engel, J. Ranft, and S. Roesler, "Hard diffraction in hadron hadron interactions and in photoproduction", *Phys.Rev.* **D52** (1995) 1459–1468, arXiv:hep-ph/9502319.

[33] T. Sjöstrand, "PYTHIA 8 Status Report", arXiv:0809.0303.

[34] T. Sjöstrand, S. Mrenna, and P. Z. Skands, "A Brief Introduction to PYTHIA 8.1", *Comput.Phys.Commun.* **178** (2008) 852–867, arXiv:0710.3820.

[35] "The coordinated theoretical-experimental project on qcd". http://www.phys.psu.edu/~cteq/

[36] P. Collins, "An Introduction to Regge Theory and High-Energy Physics", Cambridge University Press, 1977.

[37] B. Andersson, S. Mohanty, and F. Söderberg, "Recent developments in the Lund model", arXiv:hep-ph/0212122.

[38] **Particle Data Group**, K. Nakamura *et al.*, "Review of particle physics", *J.Phys.* **G37** (2010) 075021.

[39] A. Capella, U. Sukhatme, C.-I. Tan, and J. Tran Thanh Van, "Dual parton model", *Phys.Rept.* **236** (1994) 225–329.

[40] R. K. Ellis, W. J. Stirling, and B. Webber, "QCD and collider physics", Cambridge University Press, 1996.

[41] R. Brun, F. Bruyant, M. Maire, A. McPherson, and P. Zanarini, "GEANT3", 1987.

[42] **GEANT4**, S. Agostinelli *et al.*, "GEANT4: A Simulation toolkit", *Nucl.Instrum.Meth.* **A506** (2003) 250–303.

[43] A. Kalweit, "Definition of primary and secondary particles in ALICE", ALICE Analysis Note, November 2013, unpublished. https://aliceinfo.cern.ch/Notes/node/257

[44] **ALICE Collaboration**, K. Aamodt *et al.*, "Strange particle production in proton-proton collisions at $\sqrt(s) = 0.9$ TeV with ALICE at the LHC", *Eur.Phys.J.* **C71** (2011) 1594, arXiv:1012.3257.

[45] **ALICE Collaboration**, D. Chinellato, "Strange and Multi-Strange Particle Production in ALICE", *J.Phys.Conf.Ser.* **446** (2013) 012055, arXiv:1211.7298.

[46] **CMS Collaboration**, V. Khachatryan *et al.*, "Strange Particle Production in pp Collisions at $\sqrt{s} = 0.9$ and 7 TeV", *JHEP* **1105** (2011) 064, arXiv:1102.4282.

[47] F. Bock *et al.*, "Neutral meson measurements with conversions in ALICE in pp and PbPb collisions at 2.76 TeV", ALICE Analysis Note, November 2013, unpublished.
https://aliceinfo.cern.ch/Notes/node/217

[48] J. Kamin, "Estimating Material Budget Mismatch for TRD and TOF", ALICE Analysis Note, July 2014, unpublished.
https://aliceinfo.cern.ch/Notes/node/349

[49] **ALICE Collaboration**, G. Dellacasa *et al.*, "ALICE technical design report of the time-of-flight system (TOF)", 2000.

[50] **ALICE Collaboration**, "ALICE Transition-Radiation Detector (TRD): Technical Design Report", tech. rep., CERN/LHCC/2001–21, 2001.

[51] **ALICE Collaboration**, "Aliroot".
http://svnweb.cern.ch/world/wsvn/AliRoot/